Recent ISR Experiments at CERN

F. C. Erné

CERN

RECENT ISR EXPERIMENTS AT CERN

F.C. Erné

1. Motivation for building storage rings

Particle collisions at very high energies give us the opportunity to study particle production processes under interesting conditions, in which the dependence on the energy and the nature of one of the incident particles or of both of them is expected to be relatively small. Limiting, energy-independent production cross-sections are expected. Important questions, like the existence of new particles as quarks and intermediate bosons required by weak interaction theories form another subject of investigation.

As it is important to reach high centre of mass energies at still reasonable costs, intersecting storage rings have some advantages over conventional accelerators.

In a proton synchrotron, which is used to bombard a stationary target with incident particles, the centre of mass energy grows approximately like $E_{CM} = \sqrt{2m_p E}$; here E is the energy of the accelerated particle and m_p the target (proton) mass. The square root behaviour necessitates rather large steps in incoming energy in order to have a significant increase of centre of mass energy.

For two colliding protons moving against each other the situation is different. For a head-on collision the available energy becomes $E_{CM} = 2\sqrt{E_1 E_2}$; here E_1 and E_2 are the energies of

both colliding particles. To take a numerical example, two beams of 26 GeV, when colliding give a centre of mass energy of 52 GeV, and this corresponds to an equivalent energy of 1500 GeV on a stationary target.

However, there are not only advantages. With this method one can only accelerate stable particles (in our case protons), and the interaction rates are typically a factor 10^5 lower than with conventional accelerators.

2. Operation of the ISR and luminosity measurements

The ISR is in operation since the beginning of 1971. It consists of two rings of 300 m diameter, each slightly deformed towards a square shape, whereas one ring is rotated by 45° with respect to the other. In this way one has eight points where the beams intersect each other at an angle of about 15°. Downstream of each intersection there are eight to ten meter long straight sections available for installation of experiments before ISR magnets limit the aperture. In each of the rings beams up to 10 to 20 amperes can be stacked by repeated injection from the Proton Synchrotron. With the excellent vacuum conditions available in the CERN ISR, about 8×10^{-11} torr on the average and $\sim 10 \times$ lower at the intersections, decay rates of 2×10^{-4}/hour can be reached with such beams[1]. A sketch of the ISR and PS can be seen in fig. 1.

The ISR runs with a fixed set of beam energies 11.7, 15.4, 22.5, 26.7 and 31.4 GeV/c, for which settings of all bending and correction magnets have been adjusted to give optimum performance.

The highest beam momentum 31.4 GeV/c can only be reached after acceleration of the stacked beam from 26.7 to 31.4 GeV/c. Up to 4 amperes have been accelerated succesfully with the so called phase-displacement method. One occasionally runs the machine with stacks of different momenta.

The interaction rate can be expressed in the following quantities:

$$N_{int} = \sigma \times L$$

here σ = the cross-section for pp interactions and L in the luminosity. The luminosity can be expressed as follows:

$$L = \frac{c\, n_1\, n_2}{h\, \tan(1/2\alpha)}.$$

Here n_1 and n_2 are the line densities of the particles in ring 1 and ring 2 respectively ($n_1 = I_1/ec$). These can be determined very accurately. For 20 ampere beams $n \approx 4\ 10^{14}$. In the denominator of the expression the tangent of half the crossing angle α contains factors due to the relative velocity of the beams ($2c \cos \frac{1}{2}\alpha$), the Lorentz contraction from transverse cm motion, $\cos(\frac{1}{2}\alpha)$ and the interaction volume ($1/\sin\alpha$); furthermore h is the effective interaction height. The determination of this last number is a quite delicate operation and it determines the accuracy with which cross-sections can be measured at the ISR. Measured effective heights vary between 3 and 5 mm which is small compared with the width of the beams which depend on the momentum spread and thus the intensity. The beams are 7 cm wide if high currents are stacked.

at small angles

$$d\sigma/d\Omega_{el} = R_{el}(\theta) \;/\; L\, d\Omega .$$

After extrapolation to zero degree scattering angle one can use the optical theorem to obtain the total cross-section

$$\sigma = \frac{4\pi\hbar}{p}\sqrt{\frac{1}{1+\rho^2}}\quad \left(\frac{d\sigma}{d\Omega}\right)_{0^o}$$

Here one further makes use of the assumption that the ratio of the real and imaginary parts of the forward scattering amplitudes

$$\rho = \text{Re } f(0) \;/\; \text{Im } f(0) \quad \text{is close to zero.}$$

The group has actually measured ρ at the two lowest ISR energies from elastic scattering in the Coulomb region, and obtains an average $\rho = + 0.025 \pm 0.035$ [4)5)].

In both approaches mentioned, the errors come mainly from the measurement of the ISR luminosity, but the second method is less sensitive to errors in L since there

$$\sigma_t \alpha \quad \sqrt{d\sigma/d\Omega} \quad \alpha \sqrt{1/L}$$

In every experiment the time variation of the luminosity is continuously monitored with a separate scintillation counter system (luminosity monitor). The apparatus used by the CERN/Rome group is indicated in fig. 3. It consists of a set of scintillator

counter hodoscopes which can be brought very close to the ISR beam (down to 2 cm from the centre). Elastic scatters are identified by requiring collinearity.

The results of the measurements published up to now are shown in fig. 4, plotted vs incoming beam momentum on a stationary target. The low-energy data show a maximum and then a flattening off in the range of the Serpukhov energies. The cross-section appears to rise again in the ISR energy region. The results of a recent measurement at the highest ISR energy corresponding to 2000 GeV incident protons, by the Pisa/Stony Brook group is compatible with the trend shown (43.3 $\pm$ 0.8 mb, preliminary). The results discussed are compatible with an expression of the form $\sigma = \sigma_0 + \sigma_1 \ln(s/s_0)^\nu$ with σ_0 = 38.5 mb, σ_1 = 0.9 $\pm$ 0.3 mb, ν = 1.8 $\pm$ 0.4 and s_0 = 200 GeV, in the high energy region. The maximum rate of increase consistent with unitarity (Froissart limit) corresponds to ν = 2 with $\sigma_1 \simeq$ 60 mb[5].

The results of the total cross-section are compatible with the suggested rise from a recent compilation of cosmic ray data[6].

In the same figure one sees the behaviour of the total cross-section for $\bar{p}p$ as measured up to now. It is clearly very interesting to speculate how its behaviour will be at higher energies. According to the Pomeranchuk theorem the pp and $\bar{p}p$ total cross-sections should become equal up to a constant at infinite energy.

The figure also shows results from the CERN-Rome group where normalization from Coulomb scattering has been used[4], and an earlier measurement by the ACGHT-group[7].

It is of obvious importance to know how partial cross-

sections contribute to the total cross-section. Fig. 5 shows a breakdown into the total inelastic and total elastic cross-sections for incident momenta between 1 and 1500 GeV/c, as recently made by Morrison[8]. The inelastic cross-section is seen to rise slowly and monotically after an initial steep increase near threshold (up to 6 GeV/c). Morrison remarks that the simple parametrization $\sigma_{inel} = \alpha\, s^{\beta}$, with $\alpha = 26.2 \pm 0.3$ mb and $\beta = 0.037 \pm 0.002$ describes the data satisfactorily between 6 and 1500 GeV/c. The elastic cross-section is maximum at low energy and then falls continuously. At high energy the elastic cross-section becomes essentially diffractive. which causes an increase in σ_{el} as it is due to a shadow effect from inelastic scattering, hence the elastic cross-section rises again. A 12 ± 4 percent increase of the elastic cross-section in the ISR range can be inferred from measurements by the CERN-Rome group under the condition that also the slope parameter increases. The smooth behaviour of the inelastic cross-section vs energy suggests that the rise in the total cross-section is not necessarily due to the start of a new process at very high energies.

(ii) Elastic scattering at large angles.

The differential elastic cross-section at large angles, 30-100 mrad, as measured by the ACGHT-group[9] shows a diffraction pattern. In fig. 6 it is plotted vs the momentum transfer squared. For comparison measurements at lower incident momenta are also shown[10]. One sees that the diffraction pattern gradually develops as one goes to higher energies. It appears that the measurements are reasonably well described over many decades by an optical

model calculation by Durand and Lipes[11], based on work by Chou and Yang[12], if one takes the proton from factor as determined from electron-proton scattering as input. (dipole form factor $G_p(t) \propto (1/(1 - t/\mu^2)^2$, with $\mu = 0.71$ (GeV/c))^2. The calculated minimum is at the t value where it is found experimentally, the second minimum predicted by the model is not found however.

The measurement of such small cross-sections as indicated in fig. 6 requires a precise determination of angles and momenta of both scattered particles. A sketch of the apparatus used by the group is shown in fig. 7. The trajectory of each proton through one of the two large gap iron-septum magnets is defined with three sets of magnetostrictive wire chambers, of which one is placed at the centre of the magnet. The angular range covered by the apparatus is 30 - 100 mrad. Anti-counters at angles beyond this range reject a sizable fraction of inelastic events in the trigger.

A two-dimensional scatter plot of the momenta of both outgoing particles, as indicated in fig. 8, shows a peculiar pattern. One not only sees a clustering from elastic events in one dot, but also from inelastic events where one proton has retained nearly its full momentum. These events belong to an important category commonly refered to as "single diffraction excitation". We will follow this phenomenon in somewhat more detail in the inclusive measurements we will discuss next.

(iii) Inclusive measurements (CERN-Holland-Lancaster-Manchester experiment

When the ISR was under construction, it was not entirely clear that unbiassed measurements of inclusive spectra could be done succesfully. In such measurements one detects in a spectrometer one of the many particles produced in an interaction:

$$p + p \rightarrow c + ...;$$

this is commonly written as $p + p \rightarrow c + X$.

A truly inclusive measurement should impose no further conditions on the other produced particles. One nevertheless needs a way to separate the signal coming from beam-beam interactions from a background due to beam-gas interactions on the rest gas in the vacuum chamber and beam-wall interactions from interactions of the tails of the beam with the vacuum chamber. This dilemma was solved by the CHLM-group by putting their spectrometer for charged particles on top of the ISR ring and reconstructing the interaction points. As the beam heights are only a few millimeters one can reconstruct a sharply peaked interaction region on a flat background, even for particles emitted at angles as small as 30 mrad. Fig. 9 shows such a reconstruction for a 50 mrad angle. The top part gives the total number of observed events plotted vs the horizontal distance from the interaction centre. One sees a sharp peak on a very low background. The bottom part of fig. 9 is obtained by suppressing most of the beam-beam events by putting a set of counters around the opposite beam in anti-coincidence. It shows a flat background and a remainder of the beam-beam events. Background subtraction is done by extrapolating this background under the

peak. It is important to realize that the background is only so low (2 to 3%) because the vacuum conditions at the intersection are so excellent (smaller than 10^{-11} torr). This background is simply proportional to the gas pressure.

More tricky conditions for the experiment arise from occasional instabilities and blow-up of the beams, which cause large amounts of particles to collide with the beam pipes. So many secondaries are then produced that data taking has to be stopped. A rate monitor, coupled to a set of counters close to the beam pipes with an adjustable time constant of the order of a few milliseconds is used in the experiment to interrupt data taking in such cases. This may occur several times per second.

Fig. 10 shows a sketch of the 30 meter long single arm spectrometer. Two septum magnets S_1 and S_2 intercept secondary particles and steer these through a set of three bending magnets BM1, BM2, and BM3. The total maximum bending power of the five magnets is about 20 Teslameter. A trigger is provided by the scintillation counters ADFIJ. Track coordinates are measured by 21 magnetostrictive wire chambers arranged in three triplets and six doublets. Particle identification is carried out by means of three threshold Cerenkov counters; C_1 and C_2 at equal pressure (ethylene) count π and K but not p, C_3 (hydrogen) counts π only.

The first two magnets and the first two Cerenkov counters can be moved up and down and rotated in a vertical plane in order to vary the production angle between 30 and 200 mrad. The momentum range is from $\approx$ 2 GeV/c up to the maximum required $\approx$ 30 GeV/c. In this range the momentum resolution dp/p is about 1% FWHM. At one

setting the range of production angles covered is about 10 mrad, and the momentum bite accepted about 30% $\Delta p/p$.

For each run the acceptance of the spectrometer is calculated with a Monte Carlo program, which takes into account absorption, multiple scattering, decay and the shapes of the ISR beams. The systematic error in the final cross-sections is believed to be smaller than 10%.

Around the opposite beam direction at angles smaller than 200 mrad a set up of scintillators and spark chambers detects a fraction of the secondaries. These can be used to identify and subtract elastic scatters from the total measured sample. At large angles there are also setups to sample secondaries in coincidence with the particles detected in the spectrometer.

The trigger electronics is placed inside the ISR-tunnel as near as possible to the spectrometer in order to keep the delay between the passage of the particle and the application of high voltage on the spark chambers short ($\approx$ 0.5 μsec). Trigger conditions can be partially controlled from the experimental control room on top of the ISR ring by changing override signals on coincidence circuits and adjusting remote controlled delays for counter signals.

(iv) Some results

The results of inclusive measurements can be expressed in a cross-section per unit solid angle and per unit momentum of the measured energy spectrum $d^2\sigma/d\Omega dp$.

It is common however to express the data in terms of a

relativistically invariant differential cross-section

$$f_c\,(p_t, p_l, s) = E/p^2 \quad d^2\sigma/d\Omega dp = E\, d^3\sigma/dp^{\to 3} = E\, d^3\sigma/\pi dp_l\, dp_t^2.$$

Here p_l and p_t are the longitudinal and transverse components of the secondary particles detected.

Feynman[13], Yang[14] and others have greatly stimulated the investigation of inclusive spectra by predicting energy independence of this quantity as function of $x = p_l/(1/2\sqrt{s}) \cong p_l/p_{l_{max}}$ and p_t, (here $s = E_{CM}^2$) as s goes to infinity. This property is now called Feynman scaling. The statement that there is no energy dependence as a function of p_t was taken by Feynman as an empirical fact; an exponential fall-off of the cross-section with increasing p_t would account for the fact that momentum transfers between incoming hadrons would be limited by their softness, independently of their incoming energy. We will see that there is evidence that this is not 100% true and that possibly hard components show up at higher incoming momenta.

a. Proton spectra

The x-dependence of produced particles follow rather simple patterns. The proton spectra however give definite and rather detailed information on the reaction mechanisms which are important. The majority of the protons produced are relicts of the incoming protons after a process of excitation and de-excitation in which other particles have been produced. From the two incoming protons, on the average 1.4 come out of the interaction as protons. Though

baryon-antibaryon production is increasingly important at higher energies, the cross-section is still rather low at ISR energies and we can subtract its contribution to the proton spectrum under the assumption that the spectra of antiprotons and protons from these pairs are equal.

Fig. 11a represents data on invariant cross-sections $E \frac{d^3\sigma}{dp^3}$ from the CHLM and Saclay-Strasbourg groups for two values of transverse momentum p_t. As far as has been measured there is energy independence, scaling, within 10% in the entire range of x in the ISR energy range. The spectra have undergone substantial changes with respect to data at lower energies (PS data at 24 GeV/c) as indicated by a line in the same figure. The cross-section for $\bar{p}$ production is indicated with white points. One remarks that a non-zero cross-section is left for x near 0, after subtraction of this $\bar{p}$ cross-section. In fig. 11b the same data (with $\bar{p}$ subtracted) are plotted as $\frac{d\sigma}{dx dp_T^2}$ $(=\frac{\pi \sqrt{s}}{2E} E \frac{d^3\sigma}{d\bar{p}^3})$. Integration over p_t gives $d\sigma/dx$, the cross-section to slow down a primary proton to a momentum $x\sqrt{s}/2$..As far as has been measured, the p_t dependence is rather independent of x, except for $x > 0.8$, where the p_t distribution becomes steeper than for lower values of x. Therefore the two plots for fixed values of p_t should give a rather faithfull impression of what $d\sigma/dx$ looks like. One remarks three regions of interest:

i) a rather flat spectrum between $x \approx 0.2$ and 0.6, which drops off towards higher x. Such a flat x-distribution has been discussed by Hwa and Lam[15] in terms of a diffractive model. In the context of that model the flat spectrum reflects the

mass excitation spectrum of the incoming protons. A flat spectrum is also compatible with the bremsstrahlung picture introduced by Feynman.

ii) a sharp peak near $x = 1$, to be interpreted as due to single diffraction excitation, as we will see below. The high x region is quite interesting in a different context. In terms of the triple-Regge theory the cross-section near $x \approx 0.8$ can be connected with the degenerate ρ, A_2 trajectories[16], and the rise near $x = 1$ with triple pomeron exchange.

iii) at very low values of x, the cross-section $d\sigma/dx$ increases with increasing centre of mass energy, due to the factor $\frac{\sqrt{s}}{2E} \to \frac{\sqrt{s}}{2mp}$. More and more of the cross-section is thus concentrated near $x = 0$ at higher energies.

A triple-Regge description of the region has been formulated by Chan et al.[17].

We will have a close look at the end of the spectrum in fig. 12. Note that the x scale is reversed. One remarks first that the cross-section is approximately energy independent, with a possible sharpening up of the peak at higher energies. These spectra have been obtained after subtraction of elastic events by a collinearity requirement with the system around the beam opposite the spectrometer. The peak can be interpreted as due to diffraction excitation

before collision after collision

One observes the through going proton, and the momentum spectrum gives information about the missing mass in the opposite hemisphere: $M^2 \approx (1-x)\ s$.
Energy independence in x thus means that larger and larger masses are seen to be excited at higher energies. That the peak extends to $x \approx 0.9$ indicates M^2 extends to 100 and thus M to 10 GeV for $s = 1000$ GeV^2. At PS energies one sees only mass excitation up to 2 GeV.

We have made an attempt to integrate the spectrum to come to a total partial cross-section for a single-diffraction excitation. Fig. 13 shows the peak integrated over $x > 0.9$ and plotted vs p_t^2 for two ISR energies. Some small angle data from bubble chamber measurements at NAL, normalized to our data are included in the same figure. Integration gives 5.4 ± 1.0 mb at $\sqrt{s} = 23$ GeV and 5.0 ± 1.0 mb at $\sqrt{s} = 31$ GeV. This is for the sum of the peaks at $x = +1$ and $x = -1$.

Fig. 14 shows the proton spectrum again[18], but at fixed angle. This time it is compared with the fractions in coincidence with counters at various angles. One sees that if one requires to have at least one extra particle at an angle smaller than 200 mrad around the opposite beam, about 95% of the collisions fall in that category . This means that there is practically always a small angle particle in pp collisions at high energies.

For coincident particles at large angles the coincident cross-section drops dramatically in the region $x \approx 1$. This further confirms that there is a clear separation of interaction products in the case of single diffraction excitation. For excitation to high masses the picture may not be so clear.

b) Spectra of produced particles

The spectra of produced particles look quite different from the proton spectra. The limiting distributions f(x) look somewhat like e^{-cx^2}. In the multiperipheral model such a shape is expected as the x distribution reflects the shape of the momentum transfer cut-off. For small x the spectra are flat. This flat plateau has been predicted also by Feynman[13] from analogy with bremsstrahlung and with a parton model[19].

Fig. 15 shows π^+ and K^+ spectra at a fixed value of the transverse momentum for values of x larger than 0.2.

The small x region has been measured by several groups at large angles (up to 90^o). These spectra are usually plotted vs

$$y = 1/2 \log [(E + p_l)/(E - p_l)]$$

the rapidity, in order to expand the scale of the small x region. The results for several particles are shown in fig. 16 for $p_t = 0.4$. At the left side one sees the fall off just commented upon for the large x region. But at the right side a nearly flat plateau is reached in accordance with Feynman's predictions. Close inspection reveals that the plateau still rises somewhat in the ISR region. The particles in the region of the fall-off can be found mainly at small angles, the fragmentation region.

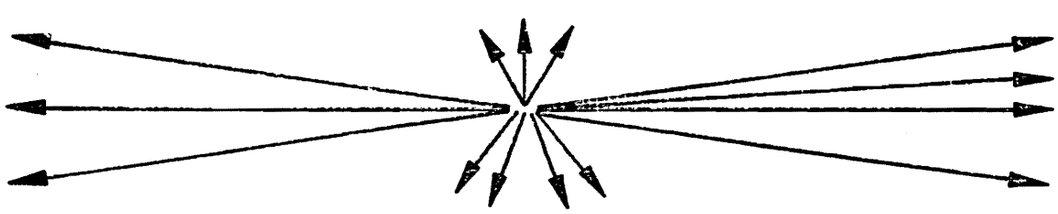

fragments 1 central region fragments 2

The small angle spectrometer thus mainly measures fragments from the incident particles. We have checked the energy independence at ISR energies for π^-, K^- and $\bar{p}$ by doing measurements at a fixed angle in the (x,p_t) plane, such that $p_t/x = 1.33$ GeV/c[29]. In this way we could cover with our spectrometer a large set of values of x at all ISR energies. In fig. 17 one sees the results for $p + p \rightarrow K^- + \ldots$ plotted as $Ed^3\sigma/d\vec{p}^3$ vs p_t (or x). The spectra are rapidly falling over several decades as both x and p_t are increasing. One observes quite a rise of the production cross-section with respect to spectra from PS energies, but in the ISR region the cross-section is constant within 10%. A similar result is found for $\bar{p}$ production, see fig. 18. One notes that the rise at small values of x is particularly large w.r.t. PS energies, but again in the ISR region there is no noticeable change.

For π^- the ISR data were coinciding so well and with such small errors that we show them only at one energy in fig. 19 and compare them with PS data again. One sees that there is perfect agreement with PS data except at large values of p_t. This is certainly connected with the fact that the phase space is quite limited at 24 GeV/c incident momentum at the PS ($p_{max} \approx 3.3$ GeV/c).

However another factor comes in, as is shown in the next figure. In fig. 20 π^+ data are shown at a fixed value of x ($x = 0.6$) plotted vs p_t, and again compared with PS data. The ISR data scale beautifully amongst themselves. One observes however that early scaling (energy independence already at low energies) only applies at small values of p_t (< 1.0 GeV/c). A similar effect is seen in the K^+ data, which are shown in fig. 21. Other groups have

measured at x = 0, the central region, and found a similar effect.

At very large transverse momenta ≈ 5 GeV/c there appears to be energy dependence even in the ISR energy region, as is found in π^o spectra measured by the CERN-Columbia-Rockefeller group[21] and shown in fig. 22. It is currently proposed that a different type of scaling should apply at very large transverse momenta. Such a scaling as function of $x_t = 2p_2/\sqrt{s}$, after division by a factor p_t^{-n}, with $n \approx 8$, would for example follow from parton models[22].

References

1) K. Johnson, Nuclear Instr. and Methods 108 (1973) 205.

2) S.R. Amendolia et al., Phys. Lett. 44B (1973) 119.

3) U. Amaldi et al., Phys. Lett. 44B (1973) 112.

4) U. Amaldi et al., Phys. Lett. 43B (1973) 231.

5) U. Amaldi, ISR results on proton-proton elastic scattering and total cross-sections, NP Internal report 73-5, 12 April 1973.

6) G.B. Yodh et al., Phys. Rev. Letters 28 (1972) 1005.

7) M. Holder et al., Phys. Lett. 35B (1971) 361.

8) D.R.O. Morrison, Review of inelastic proton-proton interactions, CERN/D. Ph. II/Phys. 73-11, 3-4-73.

9) unpublished.

10) J.V. Allaby et al., Nucl. Phys. B52 (1973) 316.

11) L. Durand and R. Lipes, Phys. Rev. Letters 20 (1968) 637.

12) T.T. Chou and C.N. Yang, Phys. Rev. 170 (1968) 1591, Phys. Rev. Letters 20 (1968) 1213, Phys. Rev. 175 (1968) 1832.

13) R.P. Feynman, High Energy Collisios (Gordon and Breach, New York 1969), Phys. Rev. Letters 23 (1969) 1415.

14) J. Benecke, T.T. Chou, C.N. Yang and E.N. Yen, Phys. Rev. 188 (1969) 2159.

15) R.C. Hwa and C.S. Lam, Phys. Rev. Letters 27 (1971) 1098.

16) M.G. Albrow et al., Nucl. Phys. B51 (1973) 388.

17) Chan Hong-Mo, H.I. Miettinen, D.P. Roy and P. Hoyer, Phys. Lett. 40B (1972) 406.

18) M.G. Albrow et al., Phys. Lett. 44B (1973) 207.

19) see also R.P. Feynman, Photon Hadron Interactions, (Benjamin, Reading 1972).

20) M.G. Albrow et al., Negative particle production in the fragmentation region at the CERN ISR, Submitted to Nuckear Physics, Febr. 1973.

21) F.W. Büsser et al., Results on large transverse momentum phenomena, presented at the Int. Conf. on New Results from Experiments on High-Energy Collisions, Vanderbilt University, Nashville, 26-28 March, 1973.

22) D. Amati, L. Caneschi and M. Testa, Large Momentum transfers and compositeness, CERN preprint, TH.1644.

Figure captions

1. Layout of the Intersecting Storage Rings (ISR).
2. Schematic layout of the hodoscope system of the Pisa-Stony Brook collaboration, used in the measurement of the total cross-section.
3. General layout of the experimental apparatus and sketch of hodoscopes in the special vacuum chamber section of the CERN-Rome collaboration for the measurement of the small-angle elastic scattering at the CERN ISR.
4. Total cross-sections for proton-proton and antiproton-proton scattering.
5. Total, elastic and inelastic cross-sections for pp scattering. The inelastic cross-sections have been obtained by subtraction of the measured elastic from the total cross-sections.
6. Comparison of the differential cross-sections of elastic proton-proton scattering at accelerator and ISR energies.
7. Experimental layout of the ACGHT-collaboration for the measurement of elastic proton-proton scattering at large $|t|$ at the CERN ISR.
8. Momentum spectra of unidentified charged particles obtained with the double-arm spectrometer from the ACGHT-group, with ISR beam energies of 26.7 GeV/c. Clustering of particles is seen in the elastic, single diffraction region and at low momenta. The charge sign is indicated by the sign of the momentum.

9. Event origins in the beam direction, reconstructed with the CHLM-small angle spectrometer at a 50 mrad setting. The top part shows all events; in the bottom part beam-beam events have been suppressed to a large extend by requiring an anticoincidence with a set of scintillator counters around the opposite beam.

10. Side and top views of the CHLM-small angle spectrometer.

11a. Invariant differential cross-section for p and $\bar{p}$ production at several ISR energies. The proton spectra are compared with measurements at lower (PS) energies, indicated by a line.

11b. Difference spectra between protons and antiprotons in the form of $\frac{1}{\pi} \frac{d^2\sigma}{dx dp_T^2}$. The measurements are from the British-Scandinavian, Saclay-Strasbourg and CERN-Holland-Lancaster-Manchester collaborations.

12. The invariant differential cross-section for the production of inelastic protons vs x for $x > 0.9$. Data at several ISR energies are compared. The experimental resolution has not been unfolded from the data.

13. The differential inelastic proton cross-section $d\sigma/dt$ vs t, integrated over the mass range subtended by the peaks at $s = 551$ and 930 GeV^2. Also indicated are NAL bubble chamber data normalized to the $s = 551$ GeV^2 data.

14. The inclusive inelastic proton spectrum at $s = 930$ GeV^2 and $\theta = 40$ mrad, and the same spectra with the additional requirement of a coincident particle in the H, V or M telescope.

15. Single particle spectra for positive particles at $s = 1995$

GeV^2 and p_T = 0.8 GeV/c.

16. The invariant cross-section plotted vs beam rapidity at p_T = 0.4 GeV/c for $\pi^{\pm}$, $K^{\pm}$, p and $\bar{p}$. The dashed lines represent data of Allaby et al. Data points come from the Saclay-Strasbourg, British-Scandinavian, Bologna-CERN and CERN-Holland-Lancaster-Manchester collaborations.

17. The invariant cross-section, measured by the CHLM collaboration for the production of negative kaons vs p_T at fixed cm angle (and hence varying x, indicated at the top scale), at three ISR energies, compared with accelerator data at s = 47 GeV^2 of Allaby et al.

18. The invariant cross-section for the production of antiprotons.

19. The invariant cross-section for the production of negative pions.

20. Distribution in transverse momentum p_T for positive pions at x = 0.6. The invariant cross-section measured in the CHLM experiment are shown at three energies. The broken line indicates an interpolation of the data at x = 47 GeV^2 of Allaby et al.

21. Distribution in transverse momentum p_T for positive kaons at x = 0.6.

22. Invariant cross-section of neutral pions at centre of mass energies of $\sqrt{s}$ = 52.7 and 44.8 GeV, as a function of transverse momentum p_T. Also shown (dotted line) is the extrapolation of low p_T data.

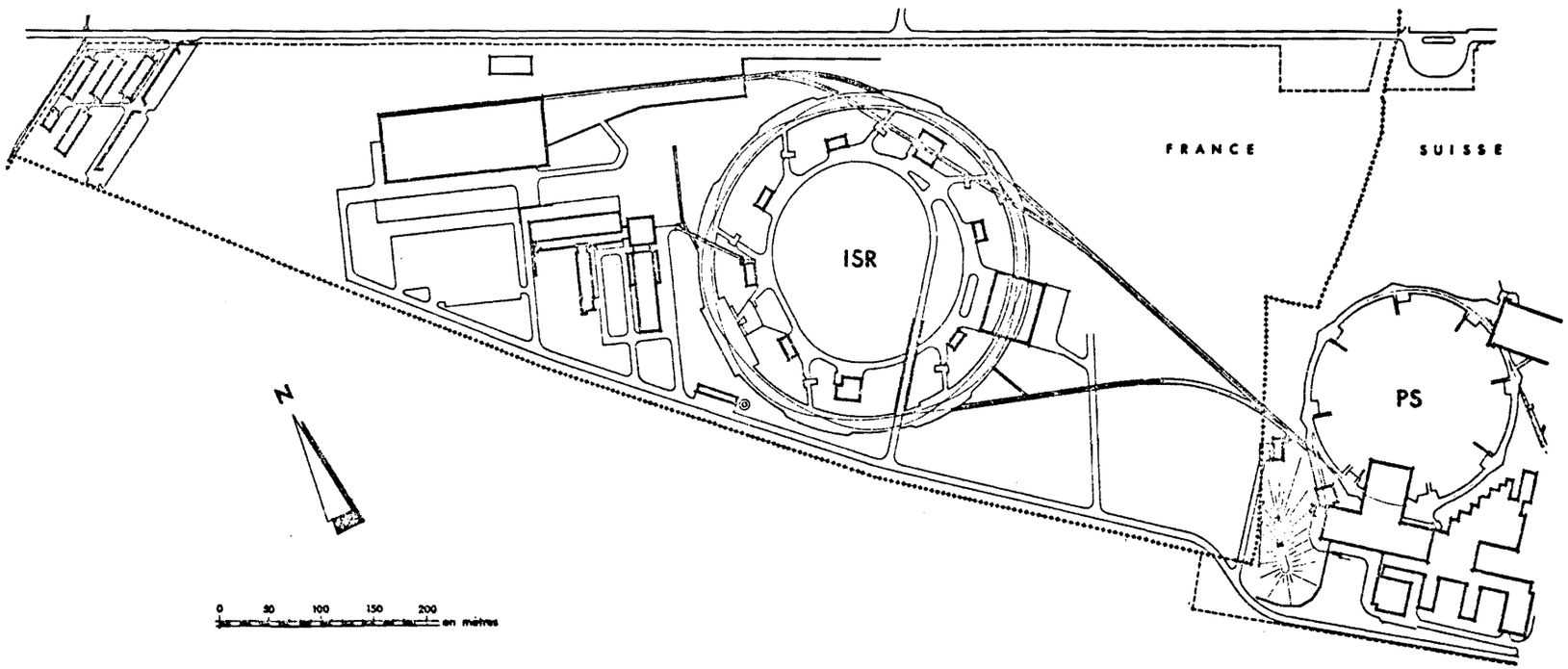

Fig. 1

PISA STONY BROOK

LAY OUT OF THE TOTAL CROSS SECTION EXPERIMENT

(TOP VIEW)

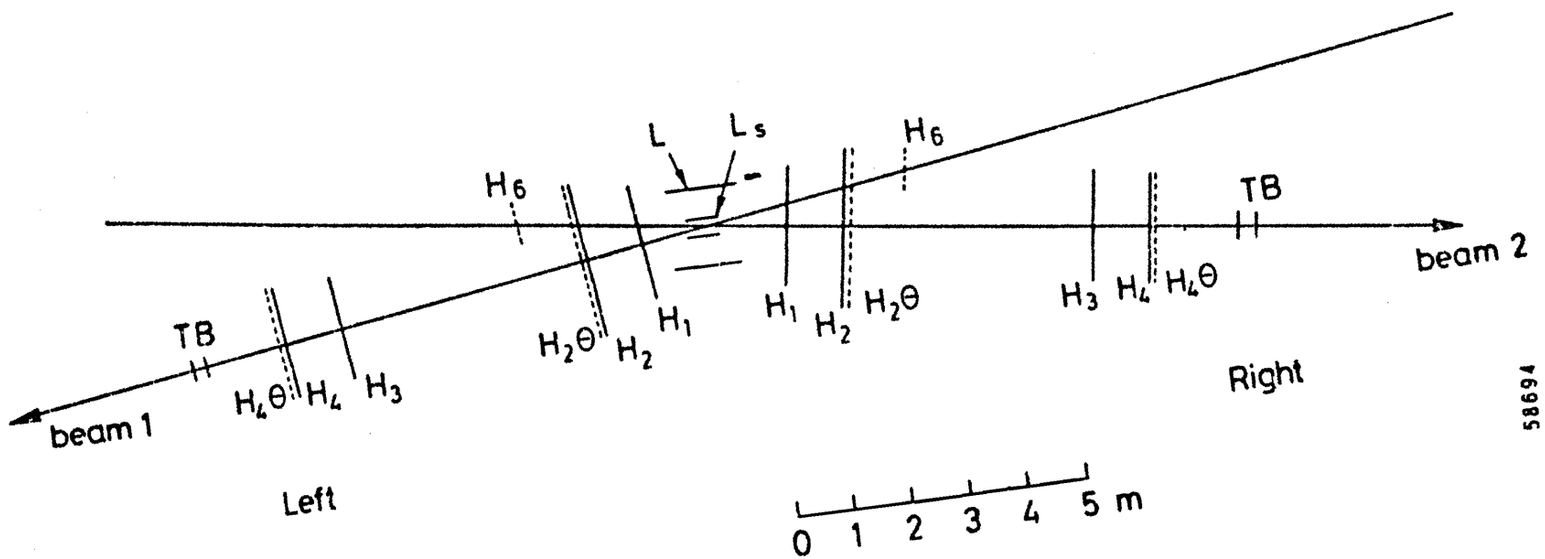

Fig. 2

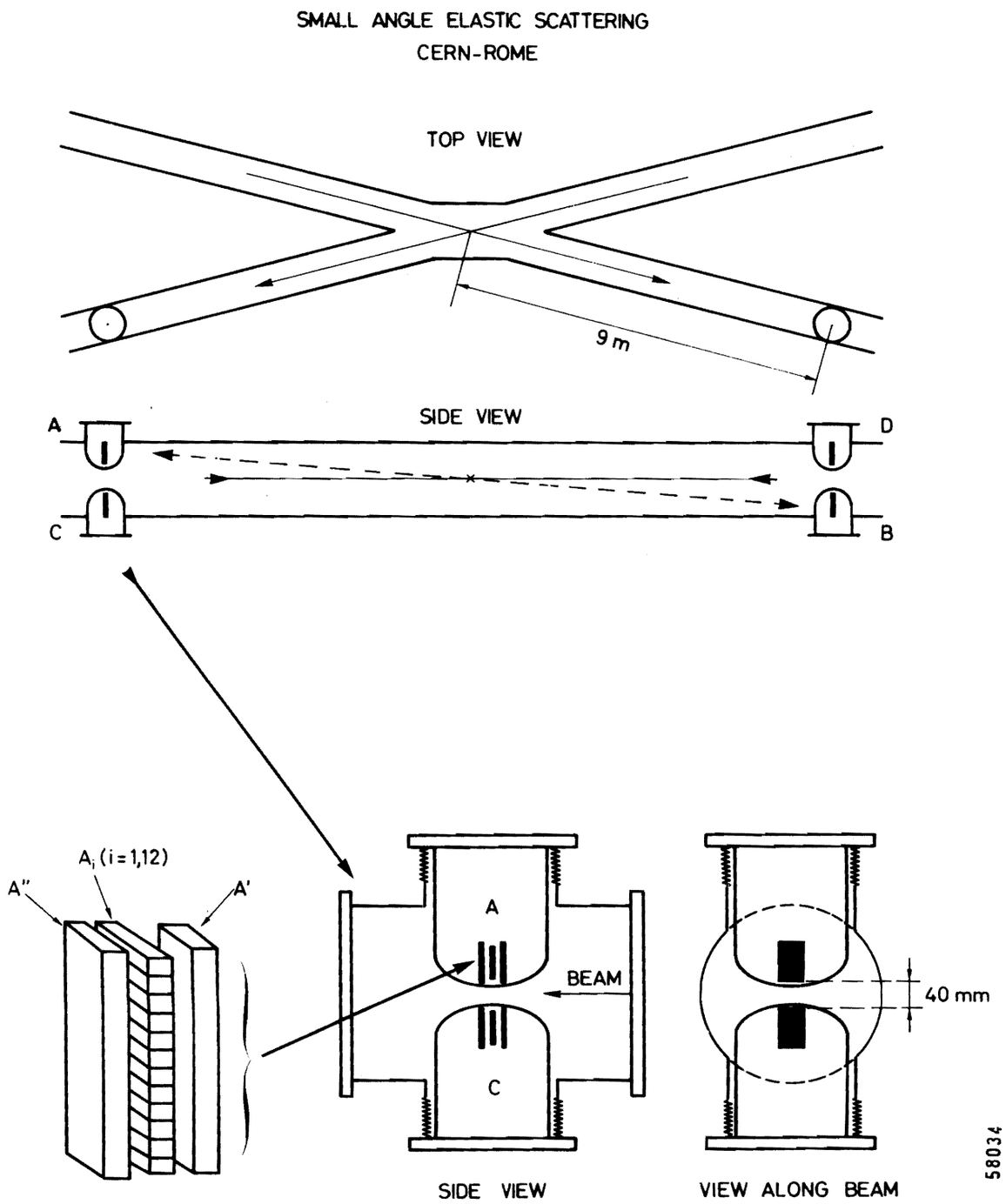
SMALL ANGLE ELASTIC SCATTERING
CERN-ROME
TOP VIEW
9 m
SIDE VIEW
A
D
C
B
A" A' A; (i=1,12)
A
BEAM
C
40 mm
SIDE VIEW
VIEW ALONG BEAM
58034

Fig. 3

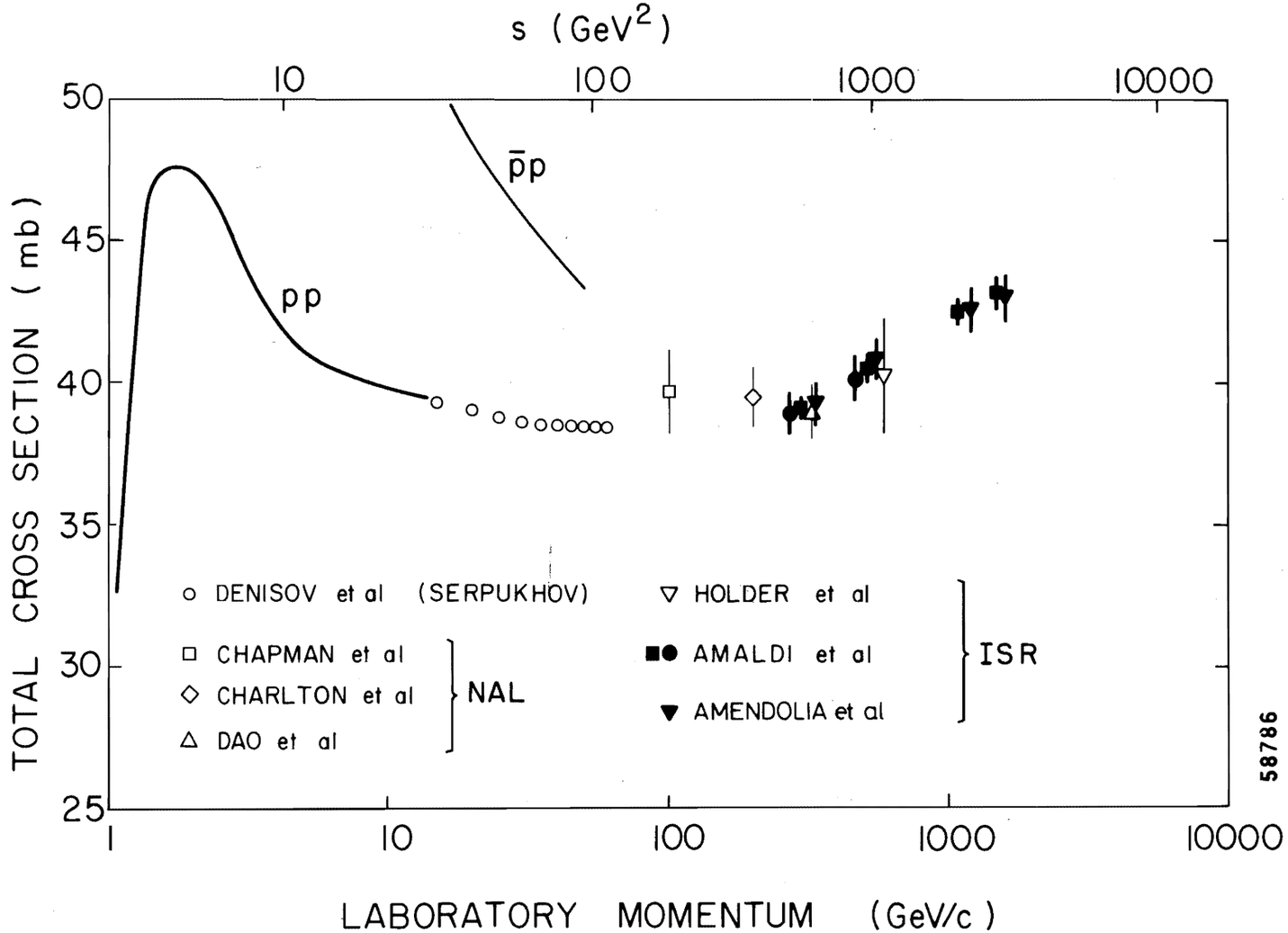
s (GeV²)
10
100
1000
10000
50
45
40
35
30
25
TOTAL CROSS SECTION (mb)
p̄p
pp
DENISOV et al (SERPUKHOV)
CHAPMAN et al
CHARLTON et al
DAO et al
NAL
HOLDER et al
AMALDI et al
AMENDOLIA et al
ISR
58786
1
10
100
1000
10000
LABORATORY MOMENTUM (GeV/c)

Fig. 4

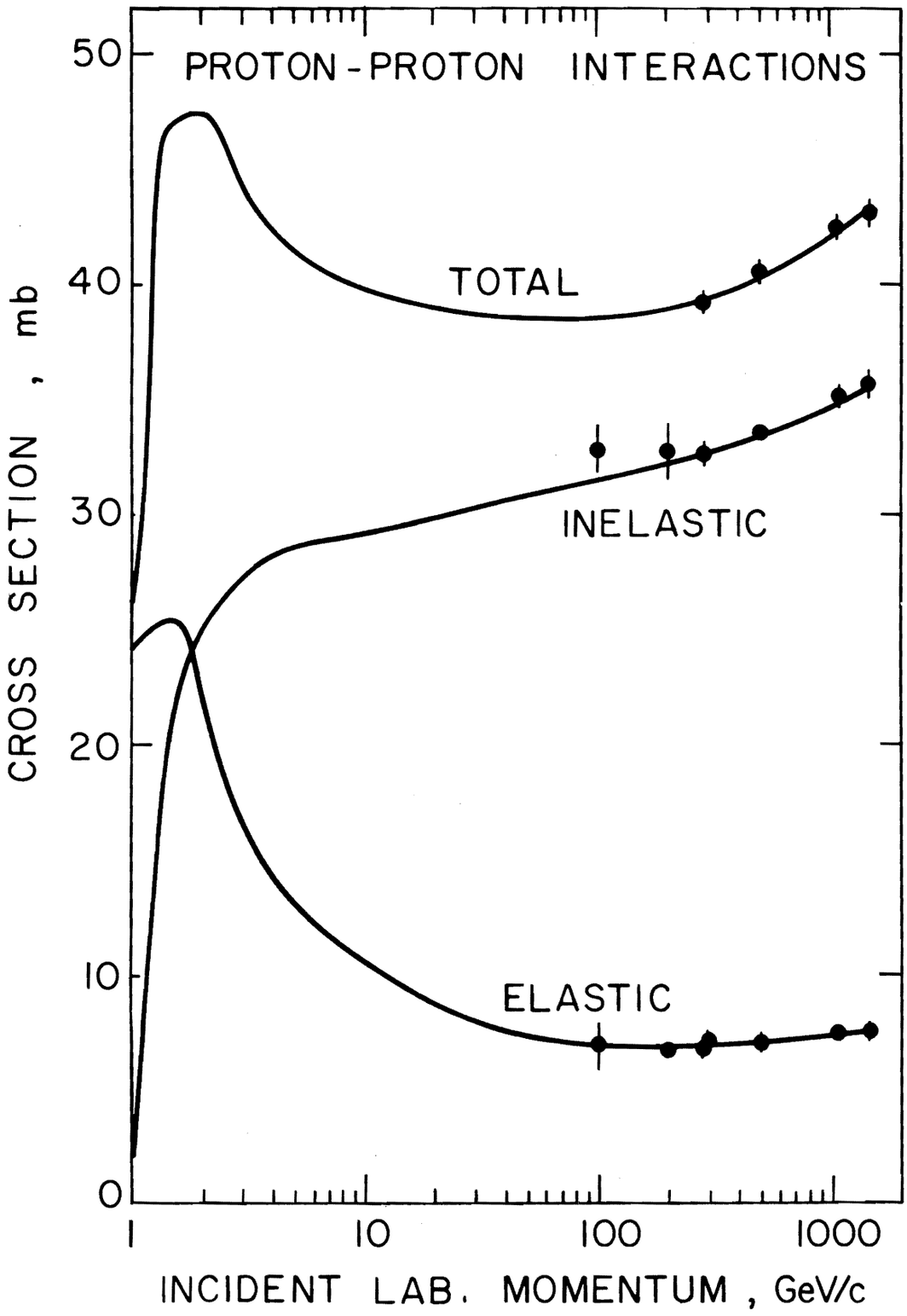
PROTON-PROTON INTERACTIONS
TOTAL
INELASTIC
ELASTIC
CROSS SECTION , mb
INCIDENT LAB. MOMENTUM , GeV/c
0
10
20
30
40
50
1
10
100
1000
58524

Fig. 5

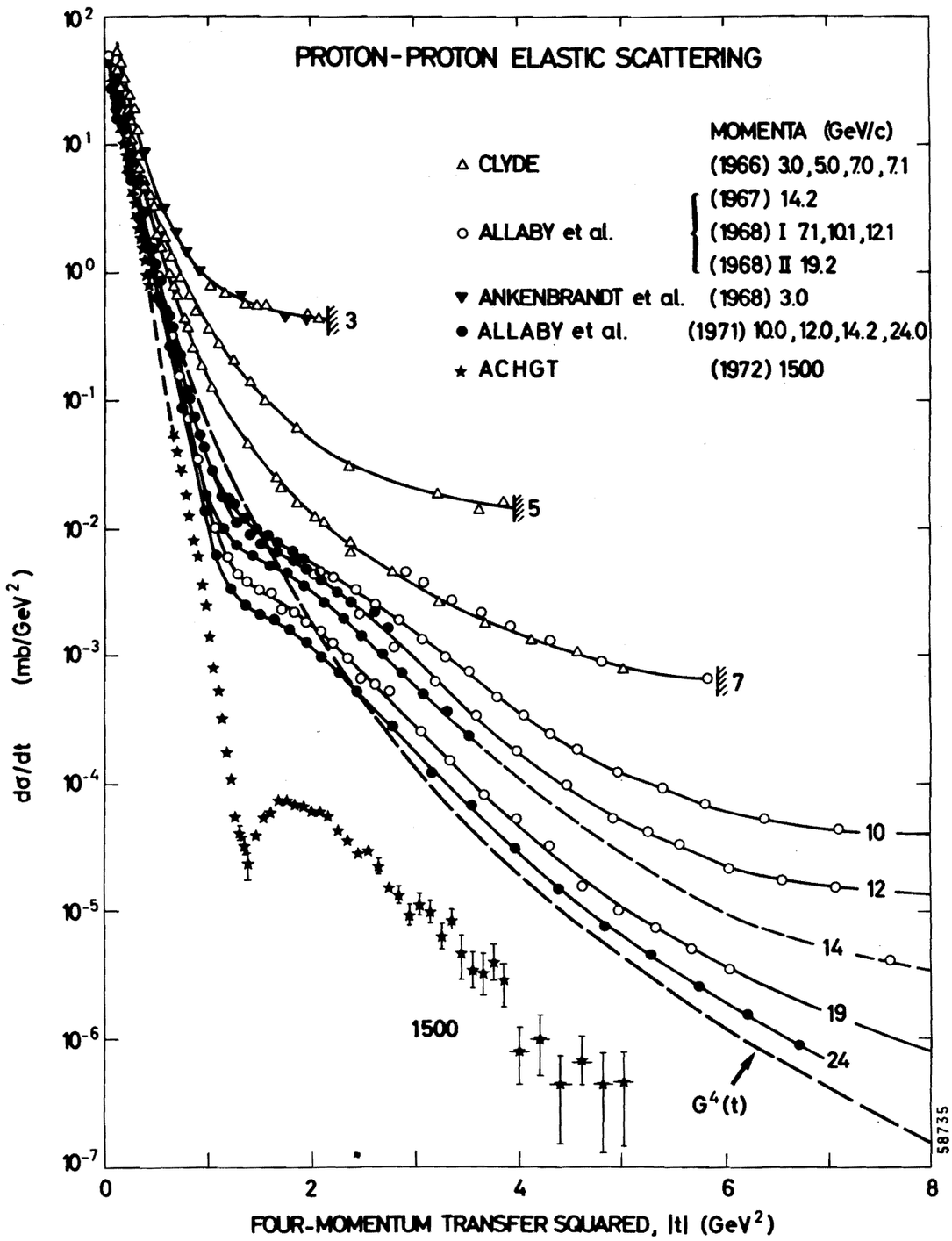
PROTON-PROTON ELASTIC SCATTERING
MOMENTA (GeV/c)
△ CLYDE (1966) 3.0, 5.0, 7.0, 7.1
○ ALLABY et al. (1967) 14.2
(1968) I 7.1, 10.1, 12.1
(1968) II 19.2
▼ ANKENBRANDT et al. (1968) 3.0
● ALLABY et al. (1971) 10.0, 12.0, 14.2, 24.0
★ ACHGT (1972) 1500
3
5
7
10
12
14
19
24
1500
G⁴(t)
dσ/dt (mb/GeV²)
FOUR-MOMENTUM TRANSFER SQUARED, |t| (GeV²)
58735

Fig. 6

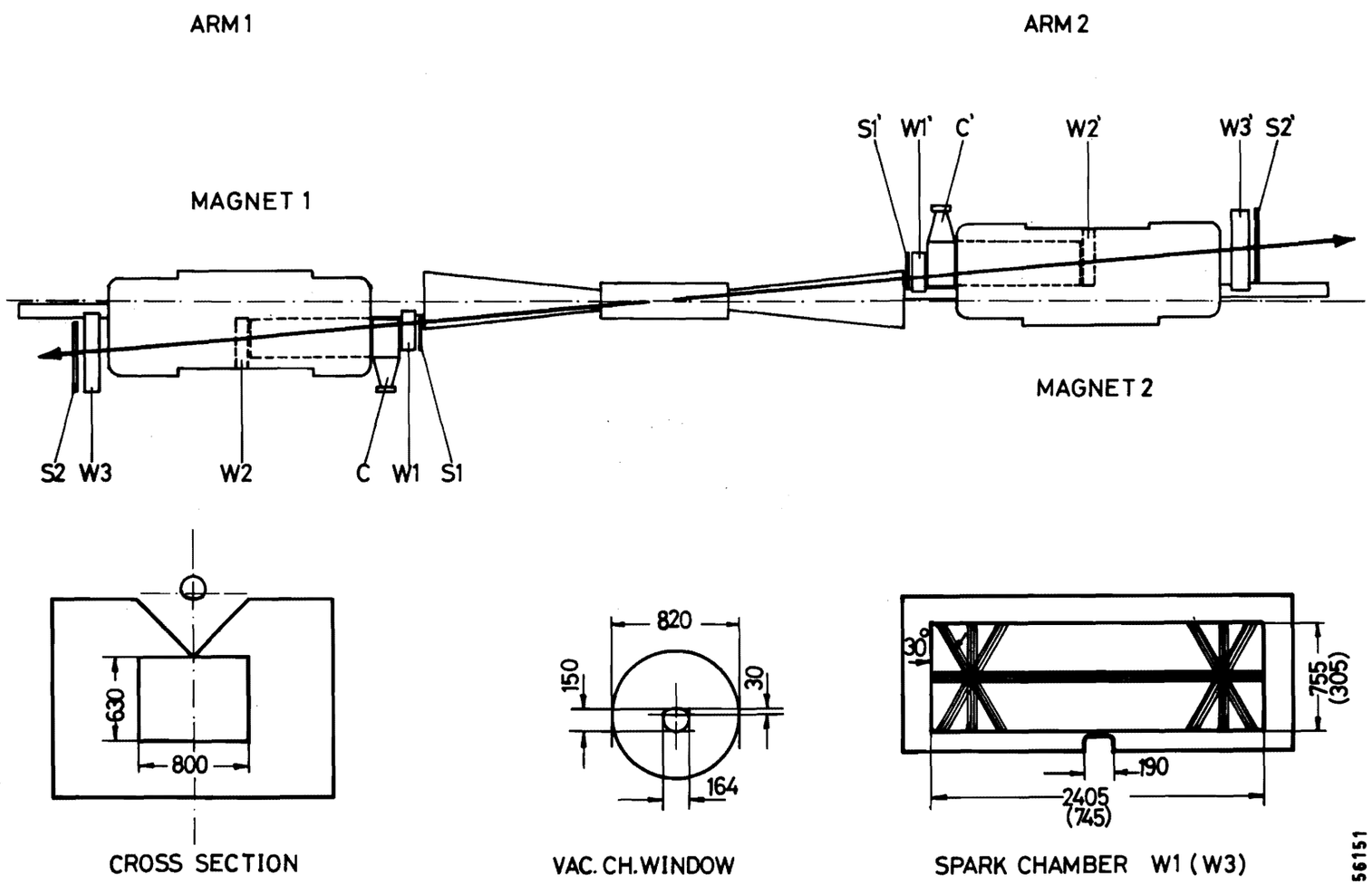
ARM 1
ARM 2
S1' W1' C' W2' W3' S2'
MAGNET 1
MAGNET 2
S2 W3 W2 C W1 S1
630
800
820
150
30
164
30°
755
(305)
190
2405
(745)
CROSS SECTION
VAC. CH. WINDOW
SPARK CHAMBER W1 (W3)
56151

Fig. 7

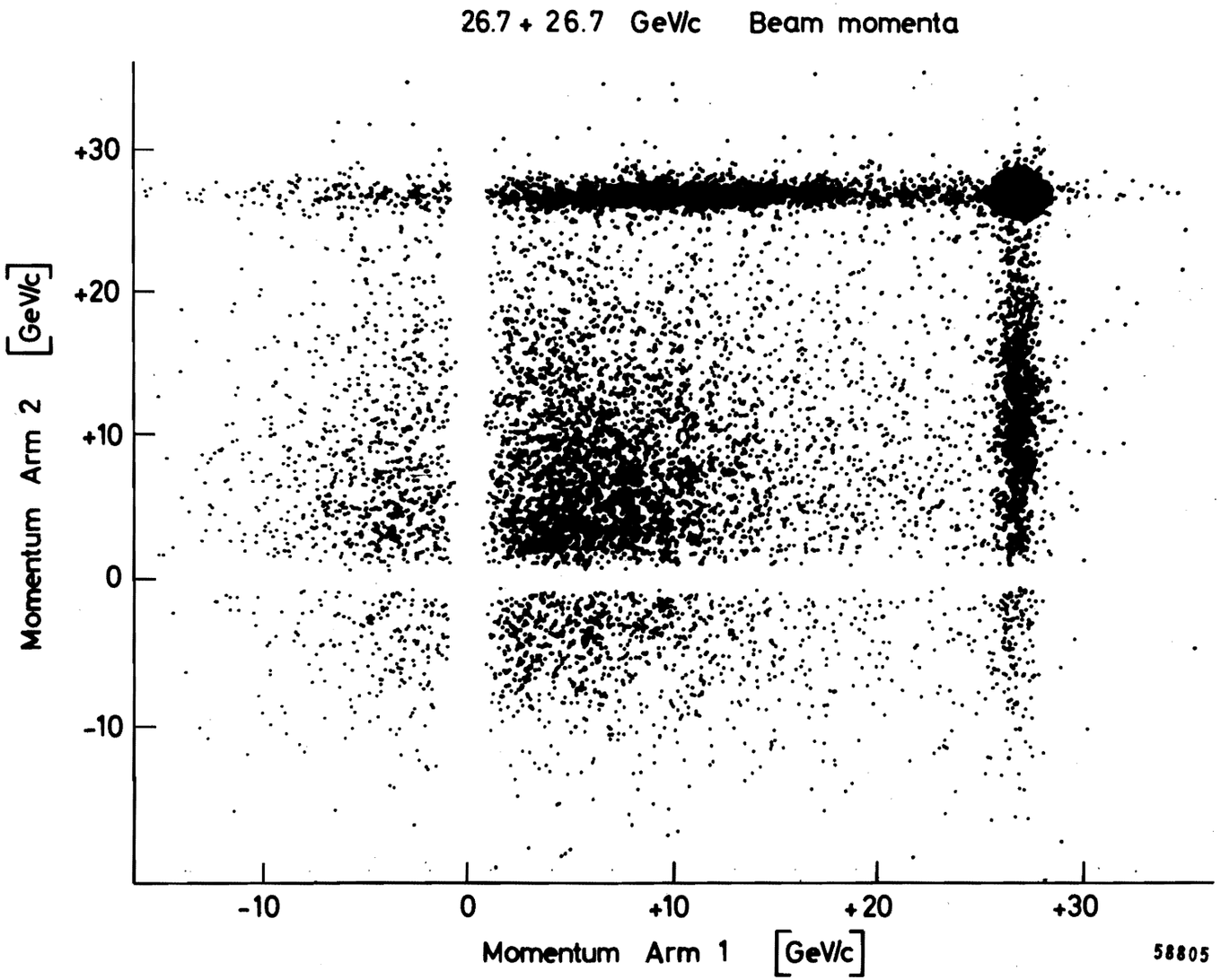
26.7 + 26.7 GeV/c Beam momenta
Momentum Arm 2 [GeV/c]
+30
+20
+10
0
-10
-10
0
+10
+20
+30
Momentum Arm 1 [GeV/c]
58805

Fig. 8

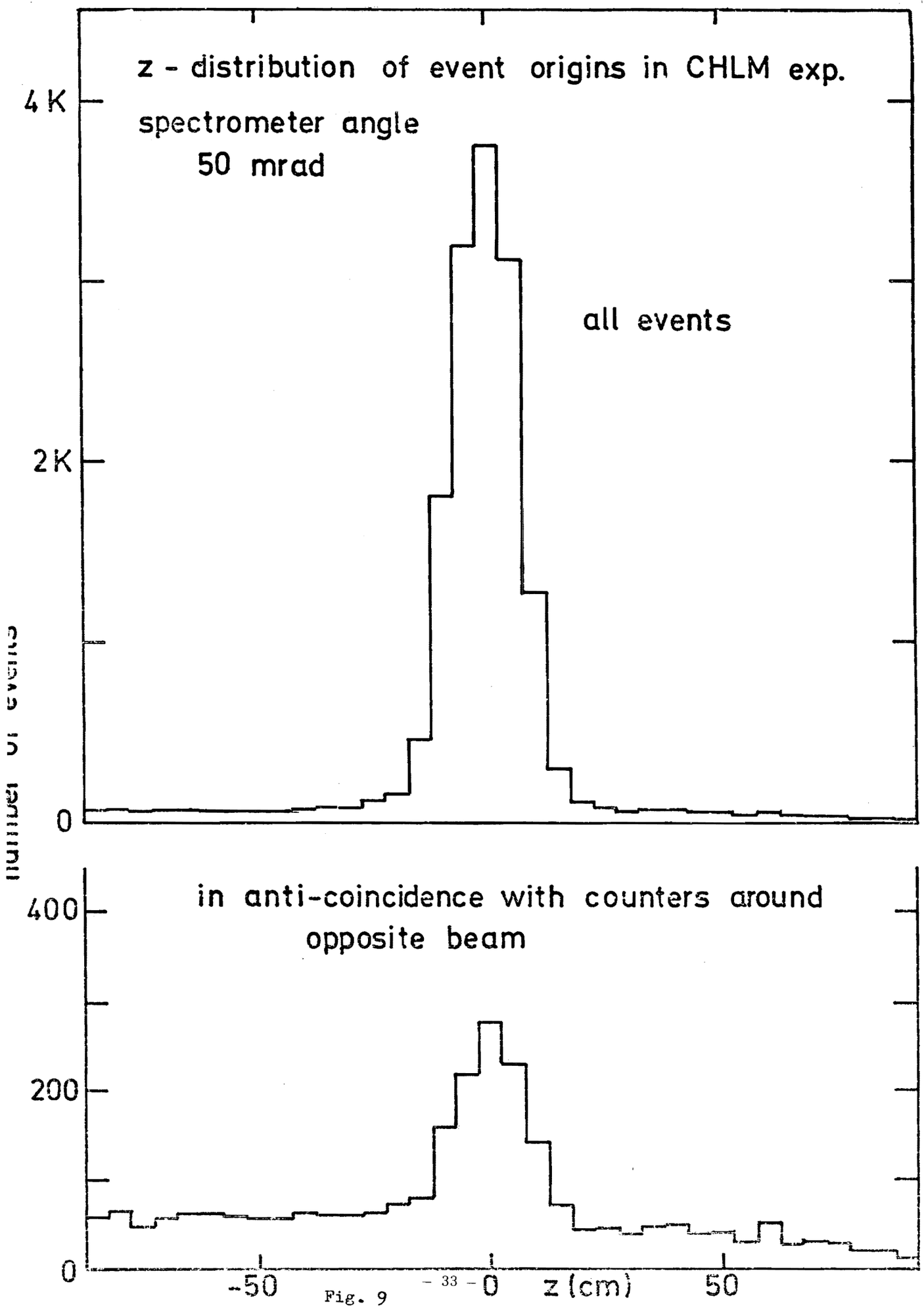
z - distribution of event origins in CHLM exp.
spectrometer angle
50 mrad
all events
4 K
2K
0
Number of events
in anti-coincidence with counters around
opposite beam
400
200
0
-50
0
z (cm)
50

Fig. 9

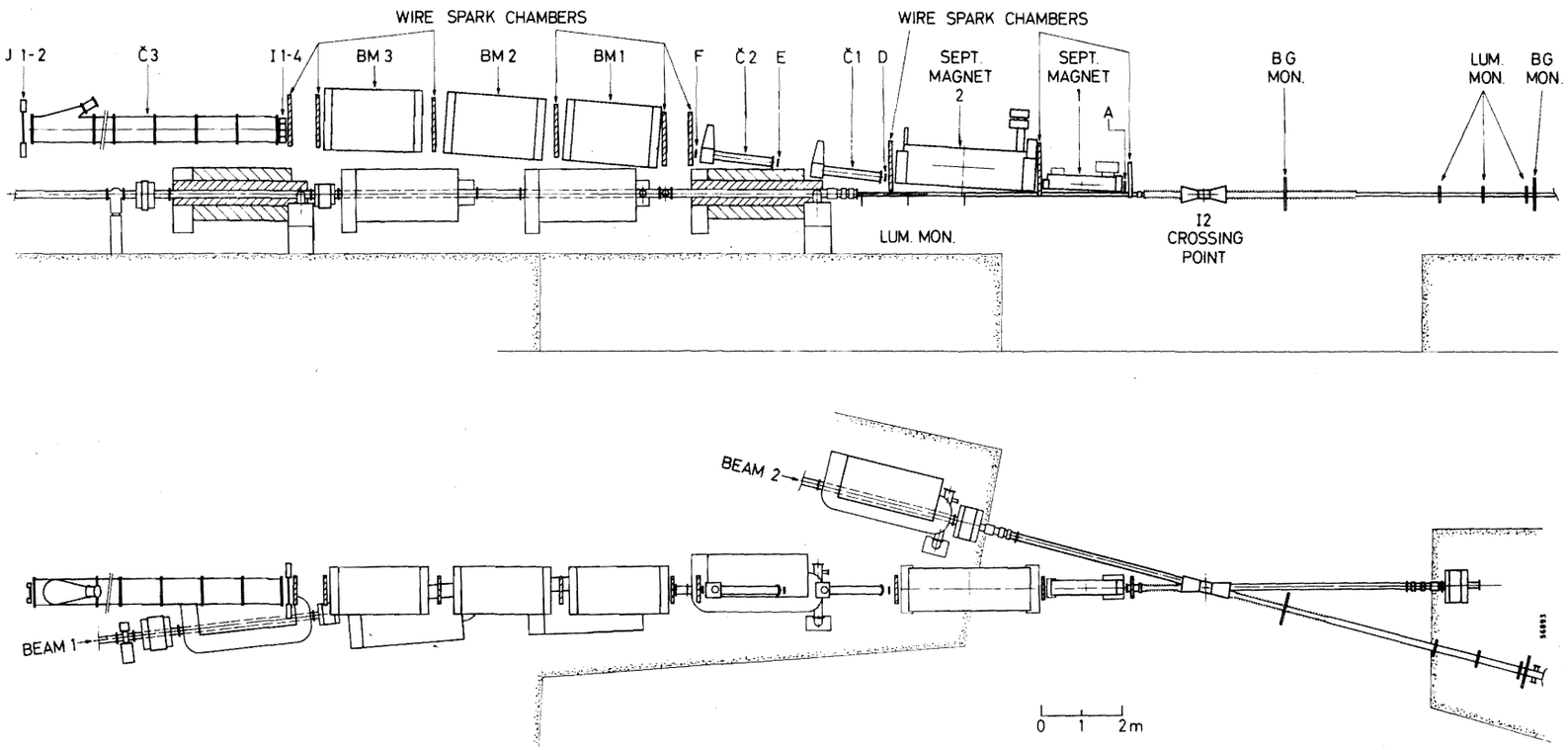
WIRE SPARK CHAMBERS
WIRE SPARK CHAMBERS
J 1-2
Č3
I 1-4
BM 3
BM 2
BM 1
F
Č2
E
Č1
D
SEPT. MAGNET 2
SEPT. MAGNET 1
A
BG MON.
LUM. MON.
BG MON.
LUM. MON.
I2 CROSSING POINT
BEAM 2
BEAM 1
0 1 2m

Fig. 10

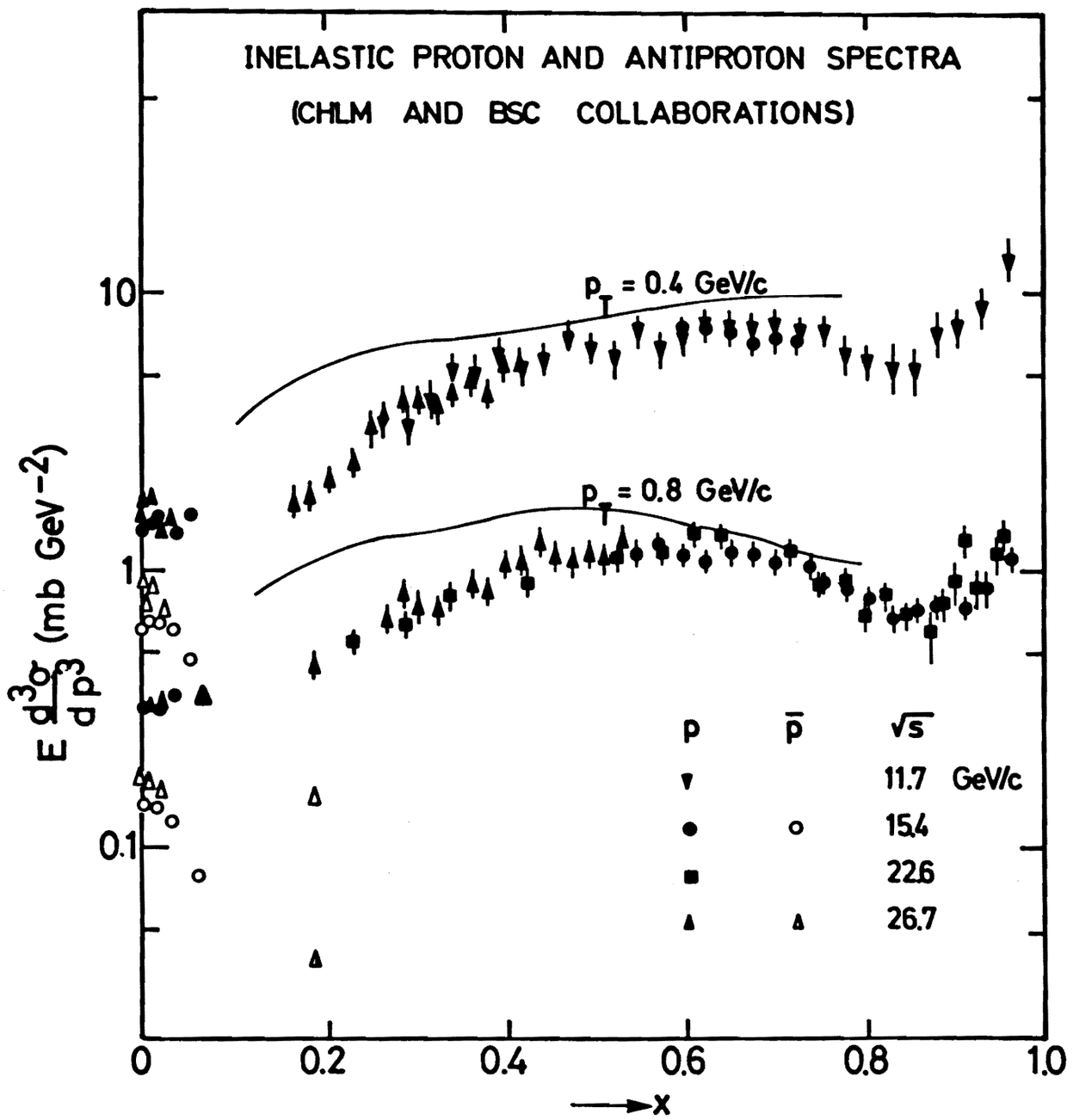
INELASTIC PROTON AND ANTIPROTON SPECTRA
(CHLM AND BSC COLLABORATIONS)
p_T = 0.4 GeV/c
p_T = 0.8 GeV/c
E d³σ/dp³ (mb GeV⁻²)
p p̄ √s
11.7 GeV/c
15.4
22.6
26.7
10
1
0.1
0
0.2
0.4
0.6
0.8
1.0
x

Fig. 11a

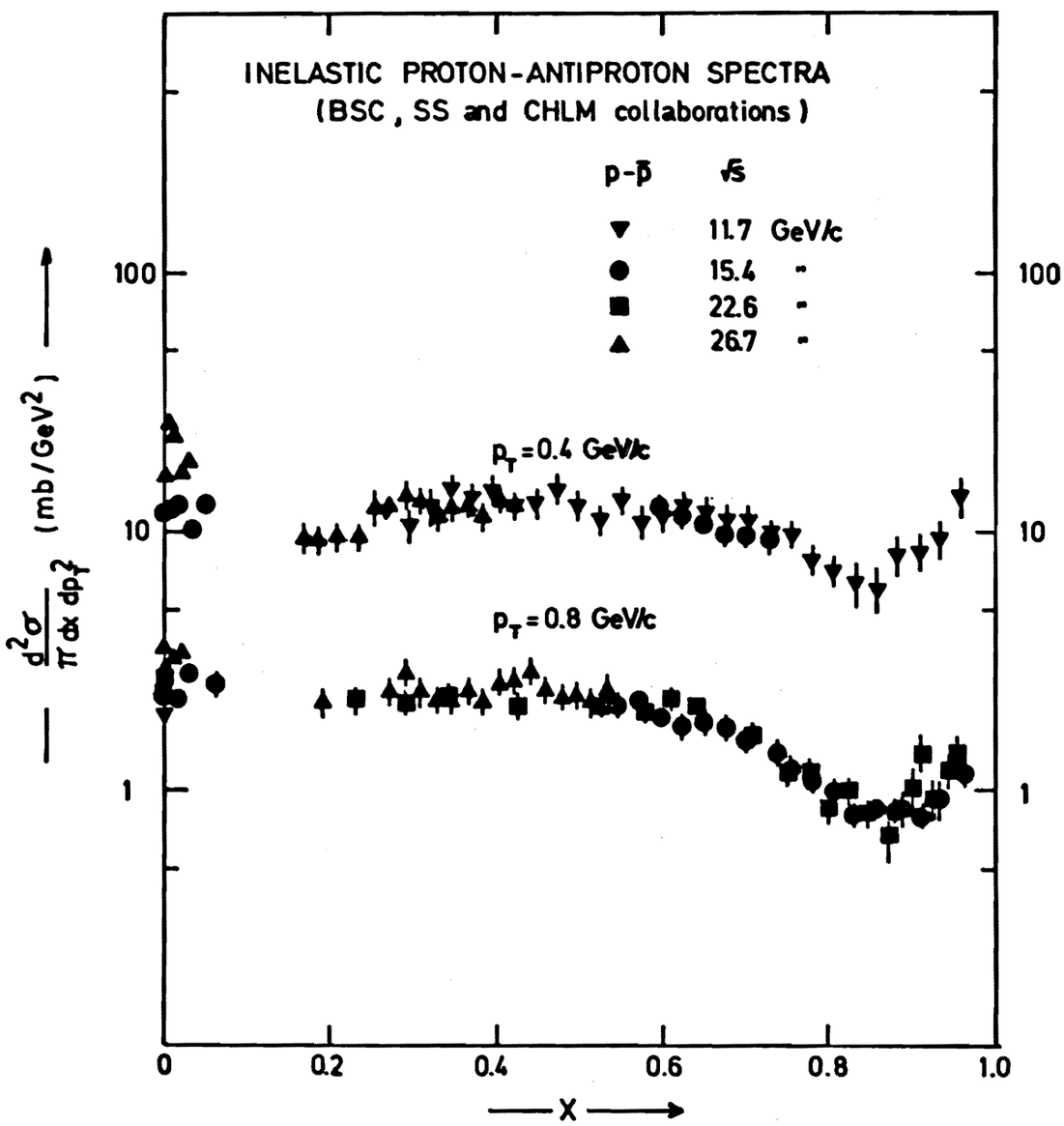
INELASTIC PROTON-ANTIPROTON SPECTRA
(BSC, SS and CHLM collaborations)
p-p̄ √s
11.7 GeV/c
15.4 "
22.6 "
26.7 "
p_T = 0.4 GeV/c
p_T = 0.8 GeV/c
100
10
1
0
0.2
0.4
0.6
0.8
1.0
X
(mb/GeV²)

Fig. 11b

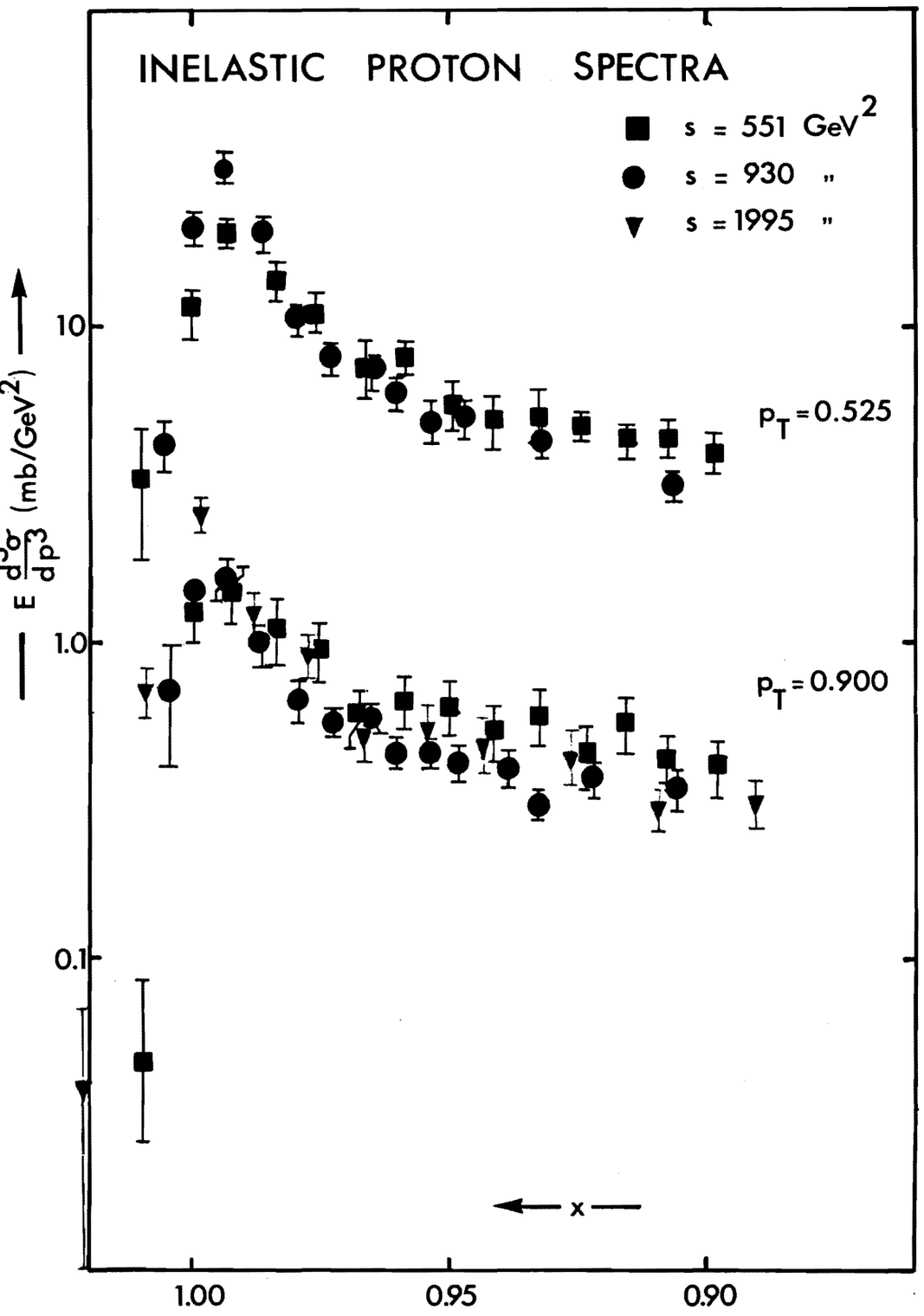
INELASTIC PROTON SPECTRA
s = 551 GeV^2
s = 930 "
s = 1995 "
$E\frac{d^3\sigma}{dp^3}$ (mb/GeV^2)
10
1.0
0.1
$p_T = 0.525$
$p_T = 0.900$
x
1.00
0.95
0.90

Fig. 12

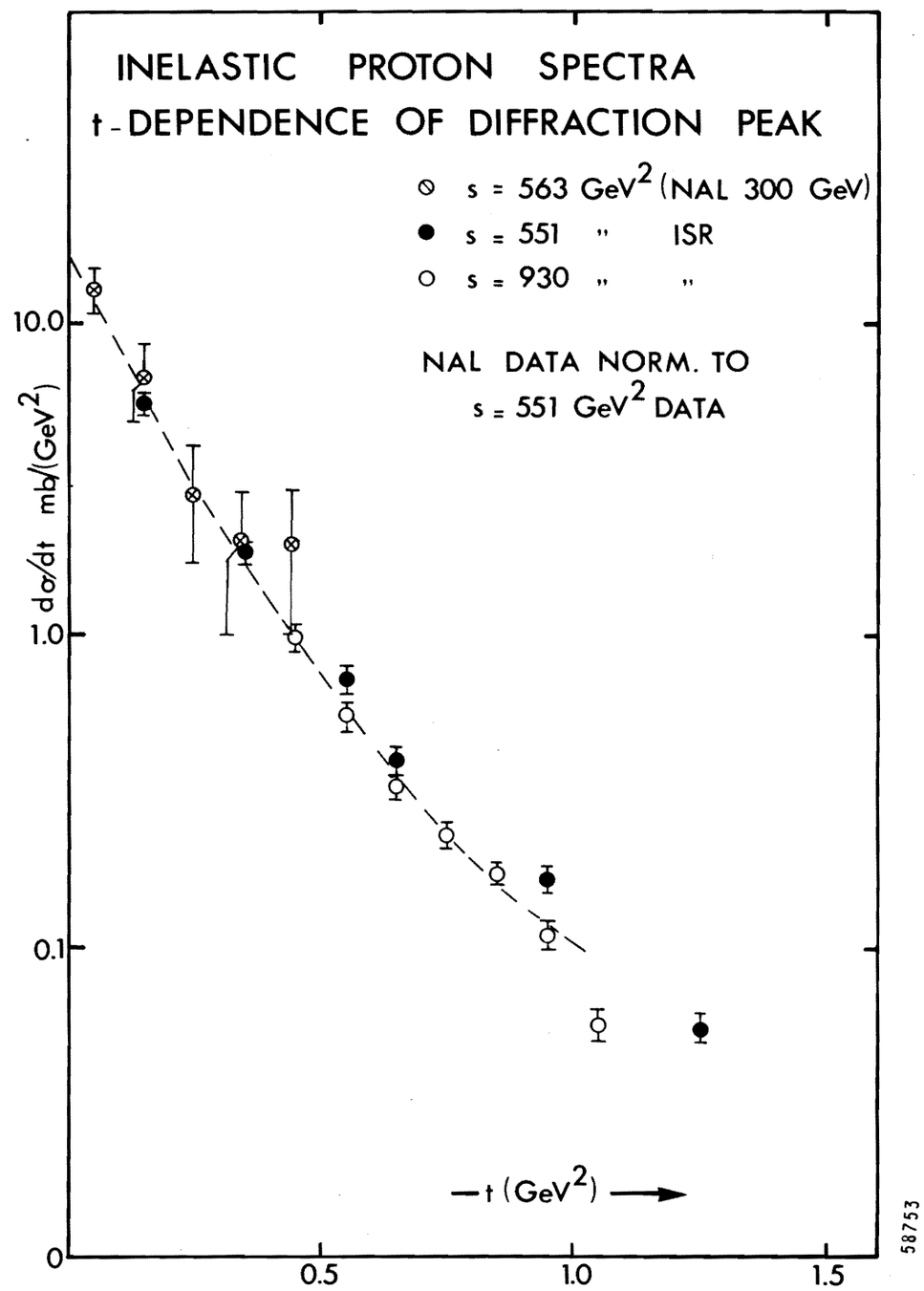
INELASTIC PROTON SPECTRA
t-DEPENDENCE OF DIFFRACTION PEAK
s = 563 GeV^2 (NAL 300 GeV)
s = 551 " ISR
s = 930 " "
NAL DATA NORM. TO
s = 551 GeV^2 DATA
10.0
1.0
0.1
0
0.5
1.0
1.5
dσ/dt mb/(GeV^2)
−t (GeV^2)
58753

Fig. 13

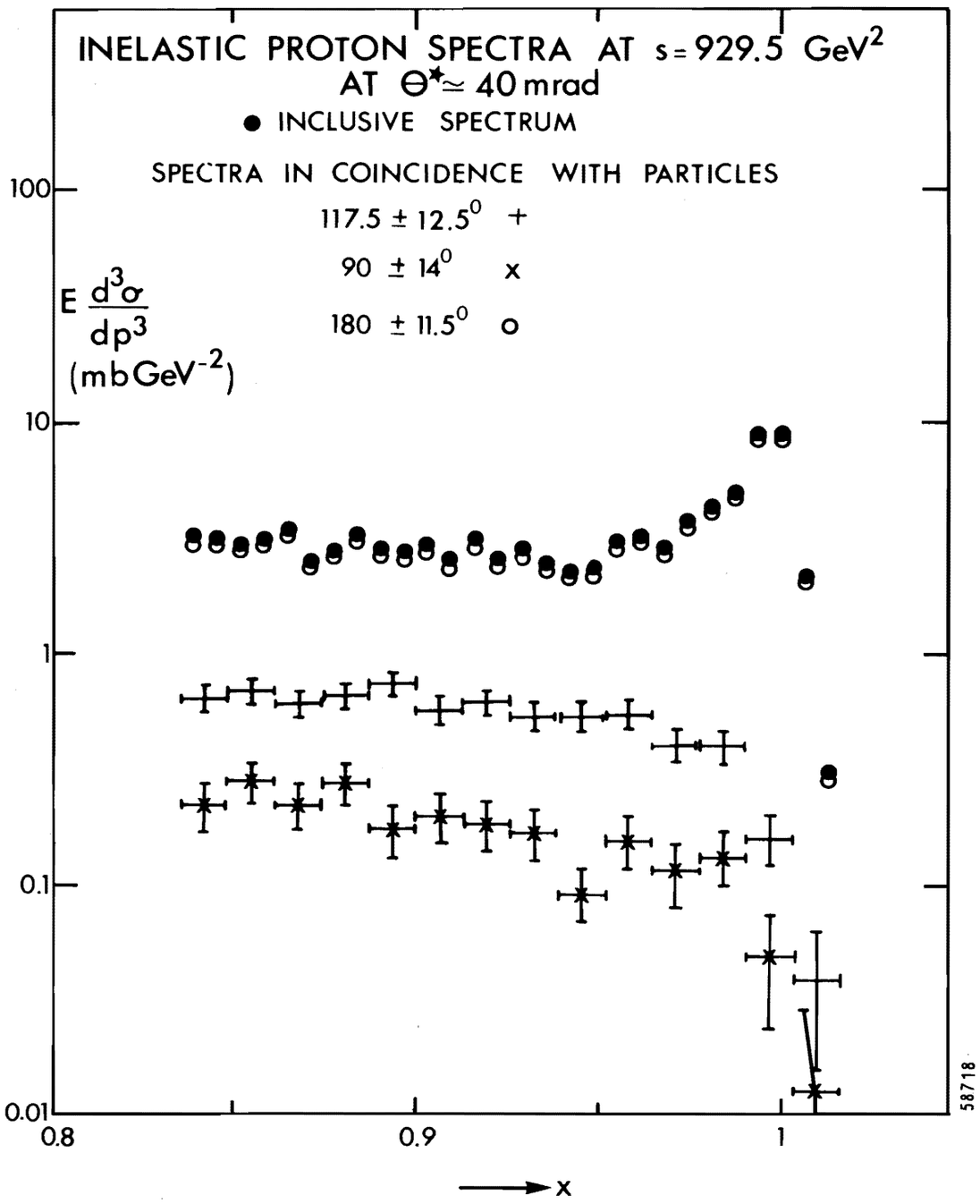
INELASTIC PROTON SPECTRA AT s = 929.5 GeV²
AT Θ* ≃ 40 mrad
● INCLUSIVE SPECTRUM
SPECTRA IN COINCIDENCE WITH PARTICLES
117.5 ± 12.5° +
90 ± 14° x
180 ± 11.5° o
E d³σ/dp³ (mb GeV⁻²)
100
10
1
0.1
0.01
0.8
0.9
1
x
58718

Fig. 14

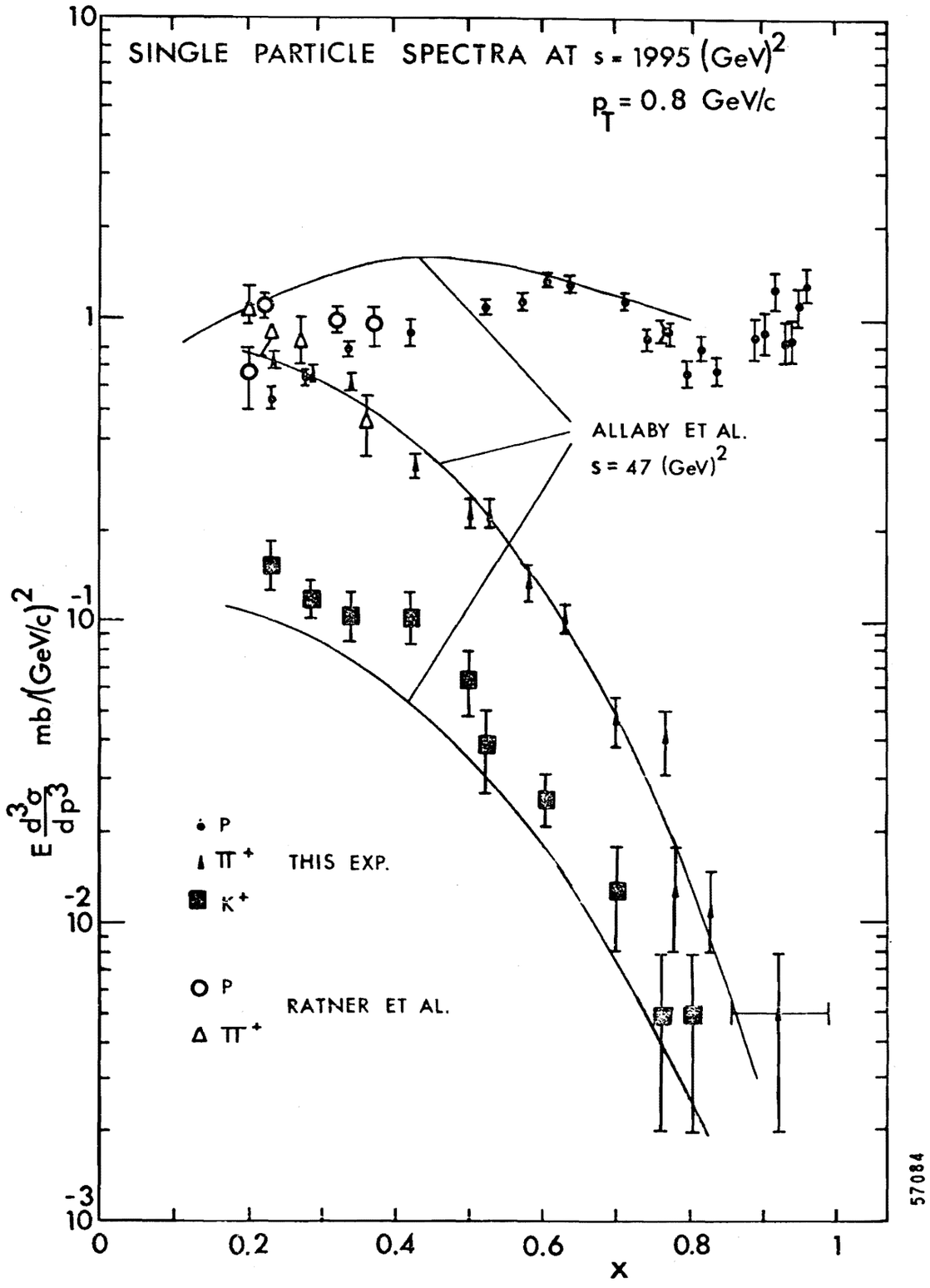
SINGLE PARTICLE SPECTRA AT s = 1995 (GeV)^2
p_T = 0.8 GeV/c
ALLABY ET AL.
s = 47 (GeV)^2
P
π^+
K^+
THIS EXP.
P
π^+
RATNER ET AL.
$E\frac{d^3\sigma}{dp^3}$ mb/(GeV/c)^2
x
10
1
10^{-1}
10^{-2}
10^{-3}
0
0.2
0.4
0.6
0.8
1
57084

Fig. 15

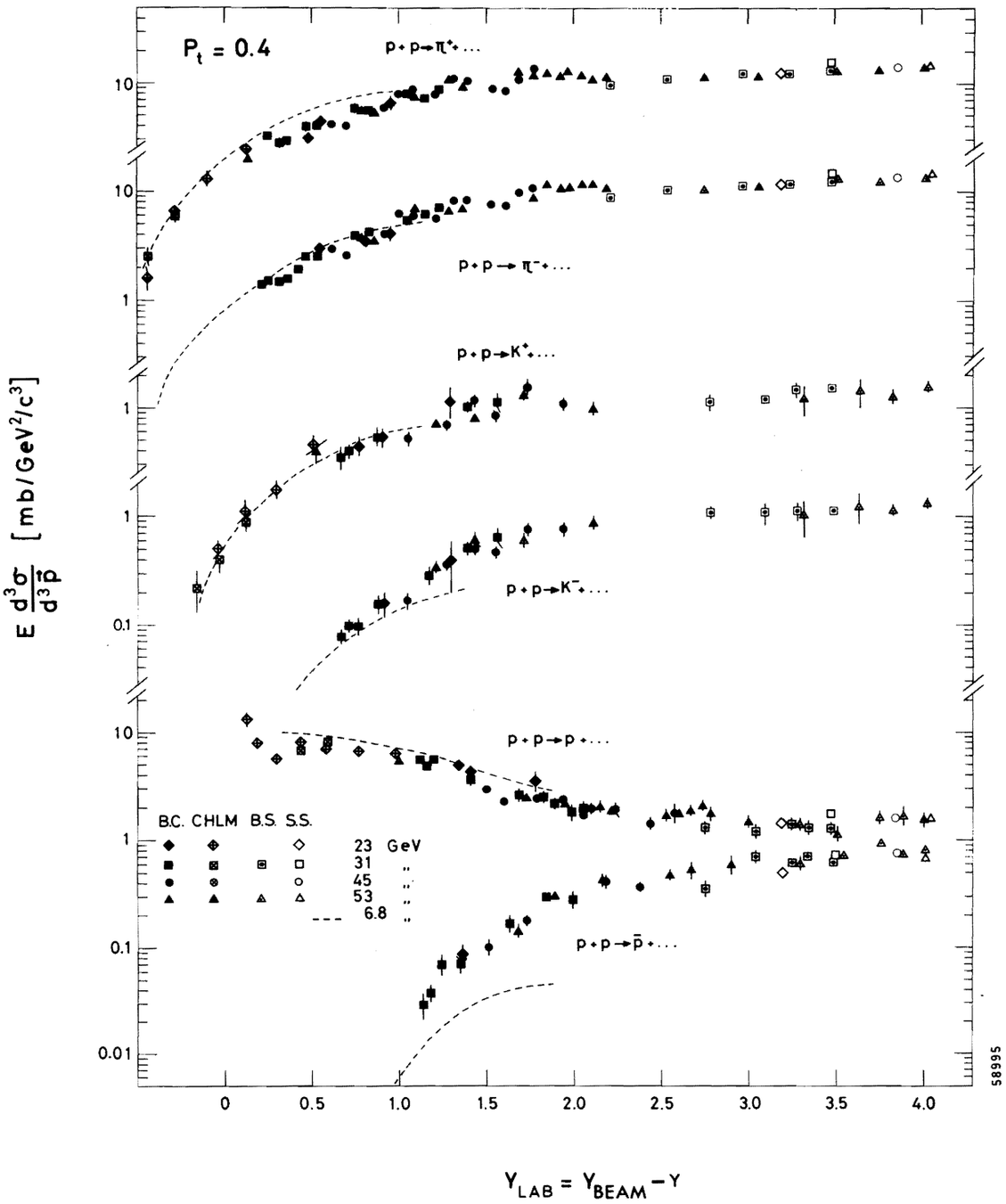
P_t = 0.4
p+p→π⁺+...
p+p→π⁻+...
p+p→K⁺+...
p+p→K⁻+...
p+p→p+...
p+p→p̄+...
B.C. CHLM B.S. S.S.
23 GeV
31
45
53
6.8
E d³σ/d³p [mb/GeV²/c³]
Y_LAB = Y_BEAM − Y
58995

Fig. 16

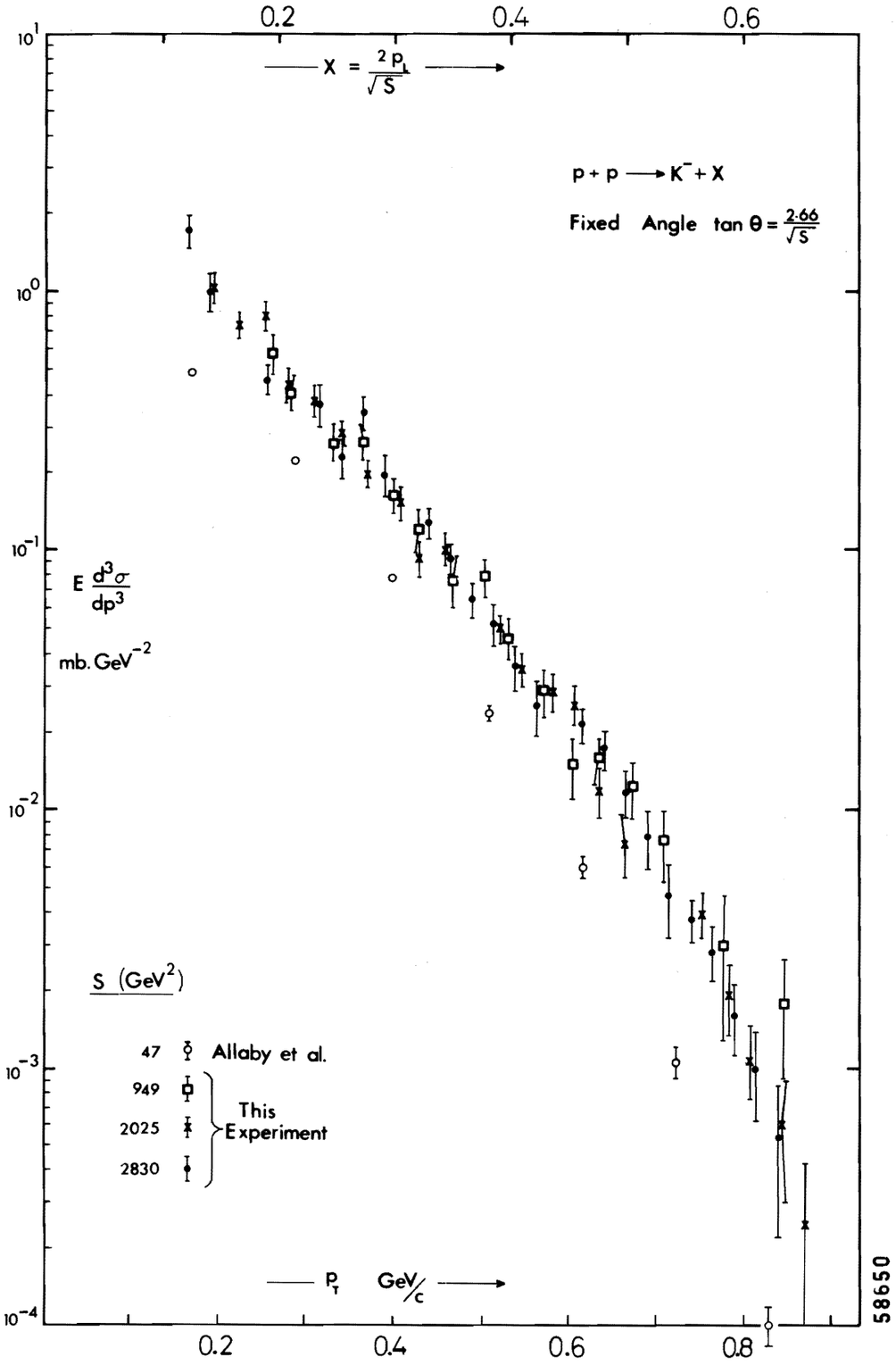
0.2
0.4
0.6
$X = \frac{2p_L}{\sqrt{S}}$
$p + p \longrightarrow K^- + X$
Fixed Angle $\tan\theta = \frac{2.66}{\sqrt{S}}$
$E\frac{d^3\sigma}{dp^3}$
mb. GeV^{-2}
10^1
10^0
10^{-1}
10^{-2}
10^{-3}
10^{-4}
S (GeV^2)
47 Allaby et al.
949
2025
2830
This Experiment
P_T GeV/c
0.2
0.4
0.6
0.8
58650

Fig. 17

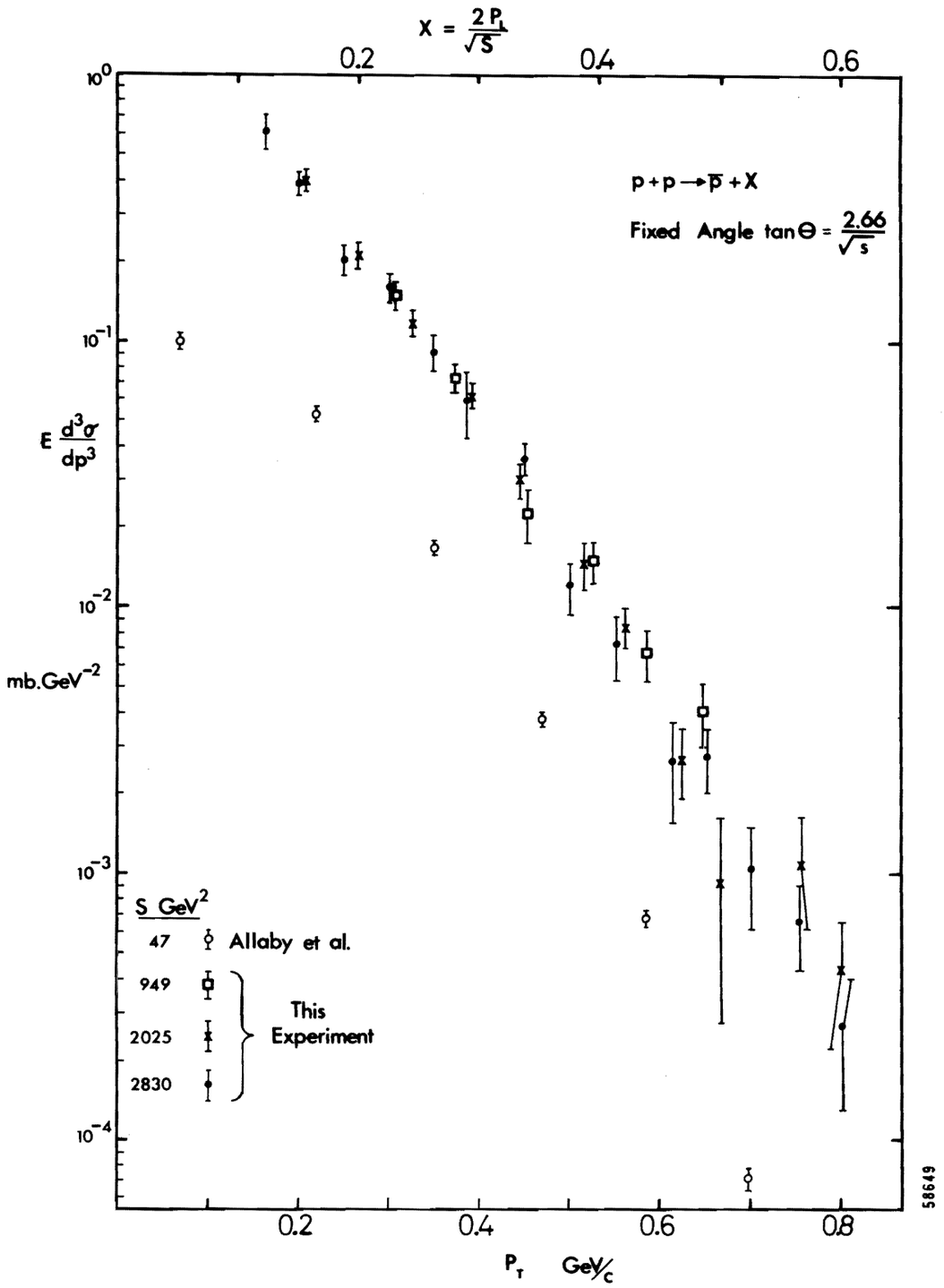
X = 2P_⊥ / √S
0.2
0.4
0.6
p + p → p̄ + X
Fixed Angle tanΘ = 2.66 / √s
E d³σ/dp³
mb.GeV⁻²
10⁰
10⁻¹
10⁻²
10⁻³
10⁻⁴
S GeV²
47 Allaby et al.
949
2025
2830
This Experiment
0.2
0.4
0.6
0.8
P_T GeV/c
58649

Fig. 18

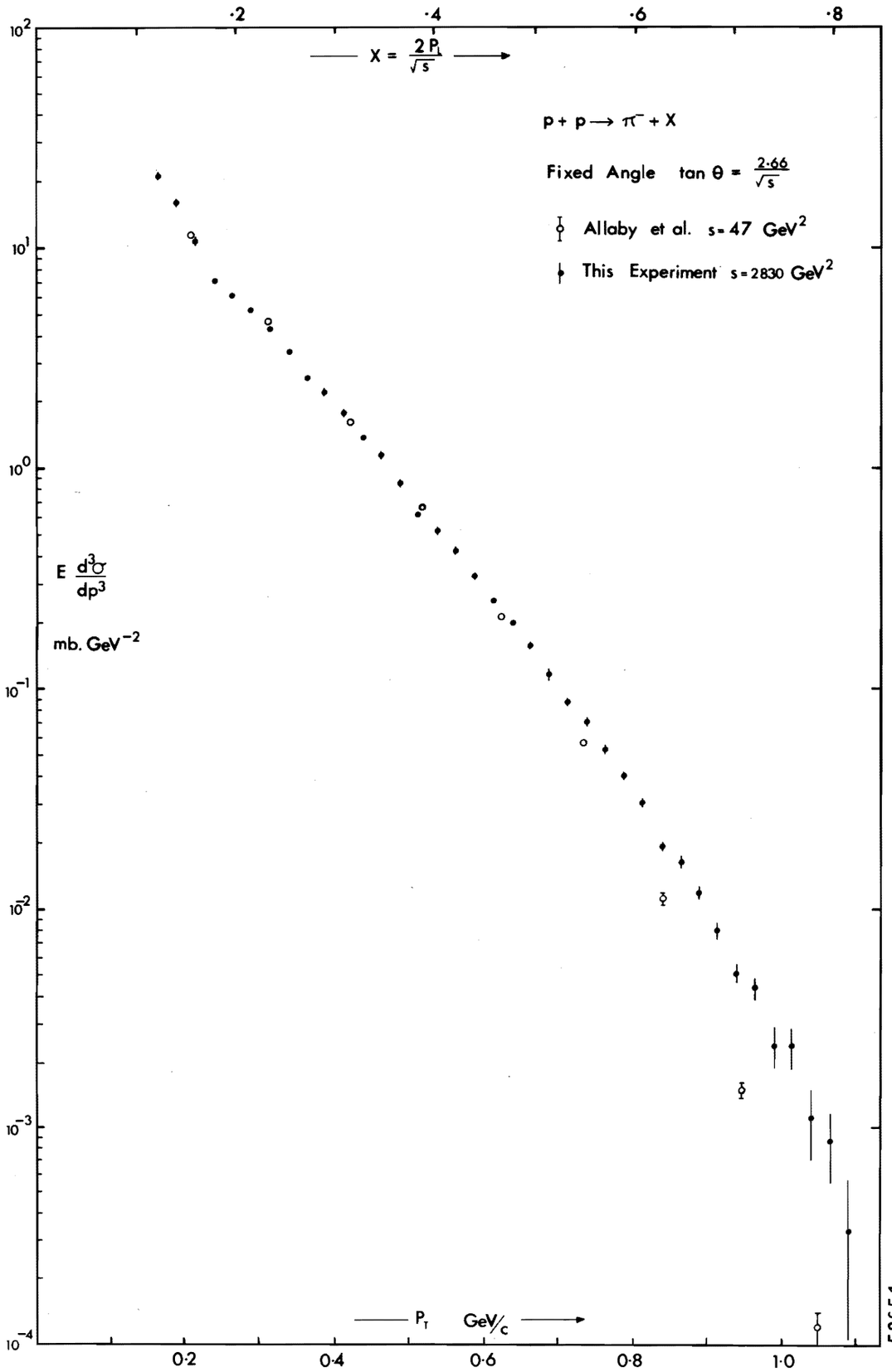
·2
·4
·6
·8
X = 2P_L / √s
p + p → π⁻ + X
Fixed Angle tan θ = 2·66/√s
Allaby et al. s = 47 GeV²
This Experiment s = 2830 GeV²
E d³σ/dp³
mb. GeV⁻²
10²
10¹
10⁰
10⁻¹
10⁻²
10⁻³
10⁻⁴
P_T GeV/c
0·2
0·4
0·6
0·8
1·0
58651

Fig. 19

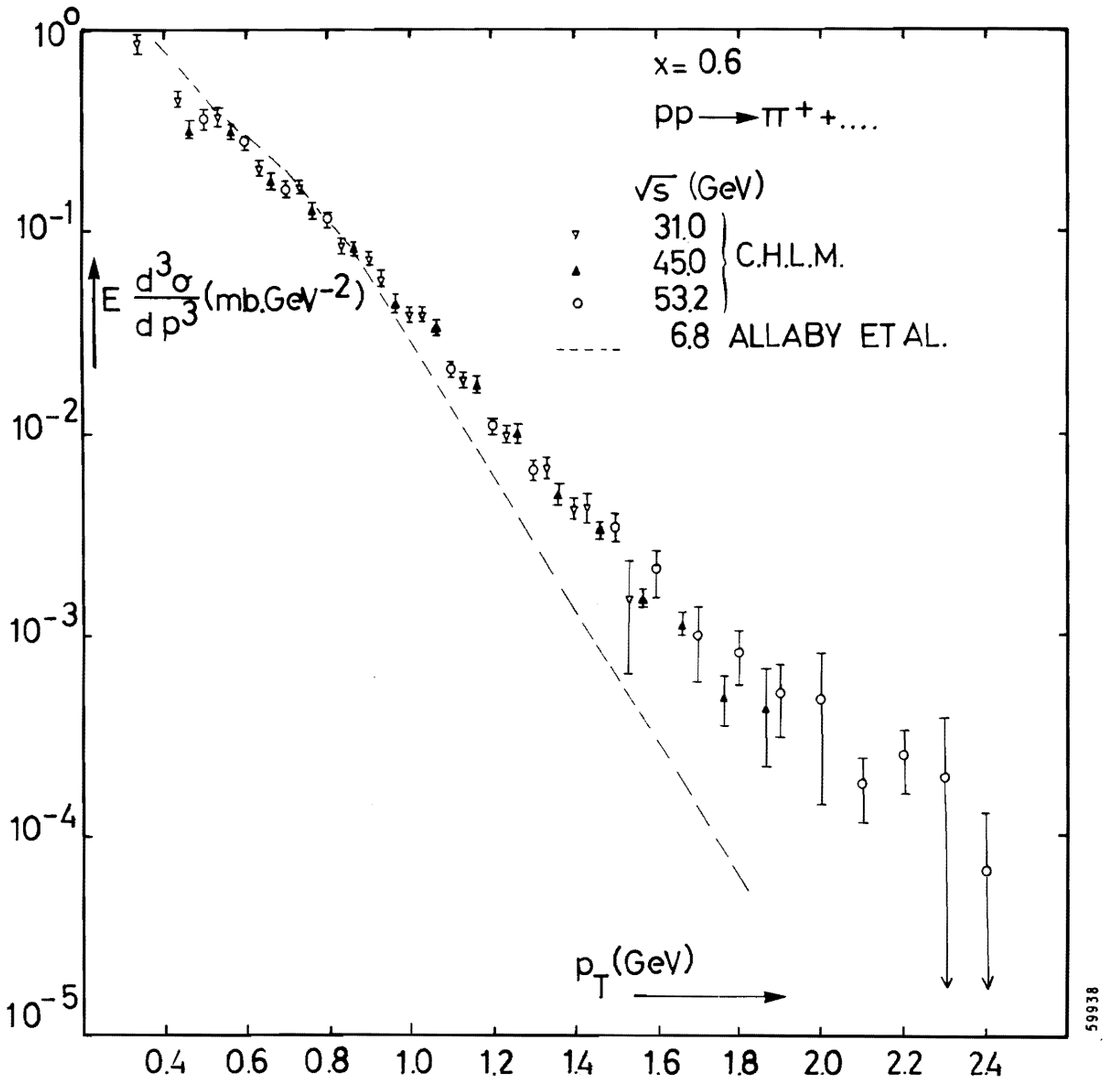
x= 0.6
pp → π⁺ +....
√s (GeV)
31.0
45.0
53.2
C.H.L.M.
6.8 ALLABY ET AL.
E d³σ/dp³ (mb.GeV⁻²)
p_T (GeV)
10⁰
10⁻¹
10⁻²
10⁻³
10⁻⁴
10⁻⁵
0.4
0.6
0.8
1.0
1.2
1.4
1.6
1.8
2.0
2.2
2.4
59938

Fig. 20

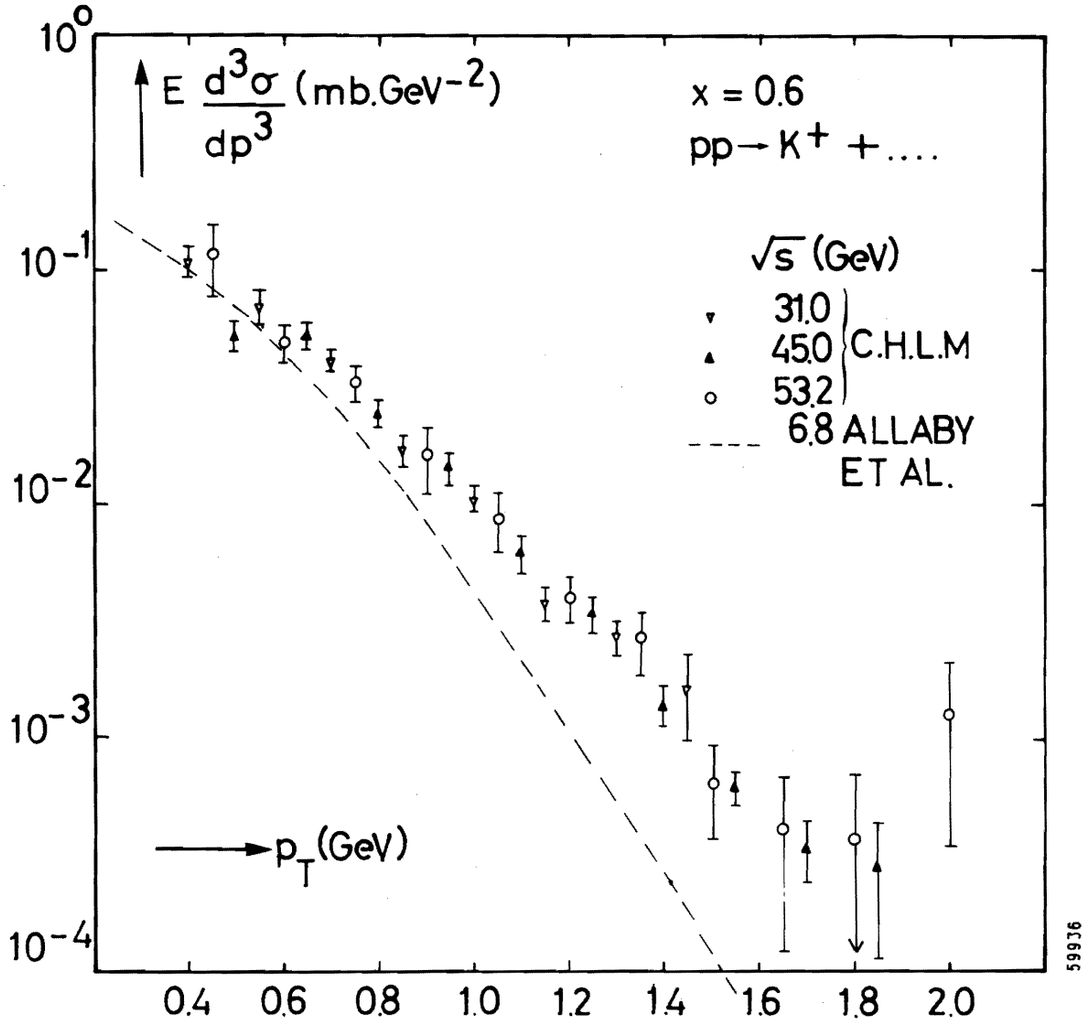
10^0
10^{-1}
10^{-2}
10^{-3}
10^{-4}
$E \frac{d^3\sigma}{dp^3}$ (mb.GeV^{-2})
x = 0.6
pp → K$^+$ + ...
$\sqrt{s}$ (GeV)
31.0
45.0
53.2
C.H.L.M
6.8 ALLABY ET AL.
p_T (GeV)
0.4
0.6
0.8
1.0
1.2
1.4
1.6
1.8
2.0
59936

Fig. 21

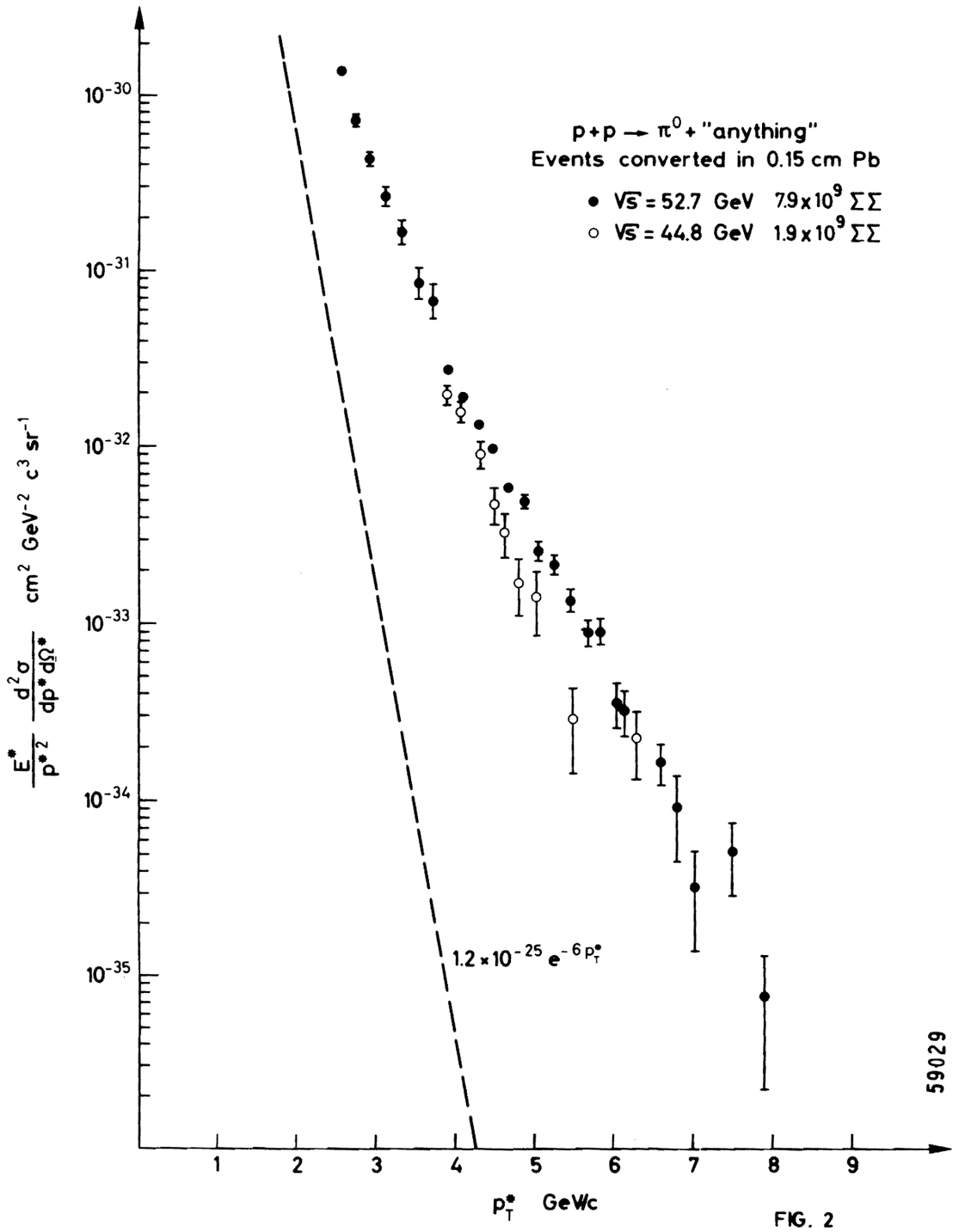
p+p → π⁰ + "anything"
Events converted in 0.15 cm Pb
● √s = 52.7 GeV 7.9x10⁹ ΣΣ
○ √s = 44.8 GeV 1.9x10⁹ ΣΣ
1.2 x 10⁻²⁵ e⁻⁶ p*T
E*/p*² d²σ/dp*dΩ* cm² GeV⁻² c³ sr⁻¹
p*T GeV/c
59029

FIG. 2

Fig. 22